



Contents lists available at ScienceDirect

Journal of Great Lakes Research

journal homepage: www.elsevier.com/locate/jglr

Comparison of satellite reflectance algorithms for estimating turbidity and cyanobacterial concentrations in productive freshwaters using hyperspectral aircraft imagery and dense coincident surface observations

Richard Beck ^{a,*}, Min Xu ^a, Shengan Zhan ^a, Richard Johansen ^a, Hongxing Liu ^a, Susanna Tong ^a, Bo Yang ^a, Song Shu ^a, Qiusheng Wu ^a, Shujie Wang ^a, Kevin Berling ^a, Andrew Murray ^a, Erich Emery ^b, Molly Reif ^c, Joseph Harwood ^c, Jade Young ^d, Christopher Nielch ^e, Dana Macke ^e, Mark Martin ^f, Garrett Stillings ^f, Richard Stumpf ^g, Haibin Su ^h, Zhaoxia Ye ⁱ, Yan Huang ^j

^a Department of Geography, University of Cincinnati, Cincinnati, OH, United States^b U.S. Army Corps of Engineers, Great Lakes and Ohio River Division, Cincinnati, OH, United States^c U.S. Army Corps of Engineers, ERDC, JALBTCX, Kiln, MS, United States^d U.S. Army Corps of Engineers, Louisville District, Water Quality, Louisville, KY, United States^e U.S. Environmental Protection Agency, Cincinnati, OH, United States^f Kentucky Department of Environmental Protection, Division of Water, Frankfort, KY, United States^g National Oceanic and Atmospheric Administration, National Ocean Service, Silver Spring, MD, United States^h Department of Physics and Geosciences, Texas A&M Kingsville, Kingsville, TX, United Statesⁱ State Key Laboratory of Desert and Oasis Ecology, Xinjiang Institute of Ecology and Geography, Chinese Academy of Sciences, Urumqi, China^j School of Geographic Sciences, Key Laboratory of Geographic Information Science, East China Normal University, Shanghai, China

ARTICLE INFO

Article history:

Received 31 March 2018

9 July 2018

Accepted 27 July 2018

Available online xxxx

Communicated by Joseph Ortiz

Keywords:

Cyanobacteria

Turbidity

Harmful algal bloom

Algorithm

Satellite

Hyperspectral

ABSTRACT

We analyzed 37 satellite reflectance algorithms and 321 variants for five satellites for estimating turbidity in a freshwater inland lake in Ohio using coincident real hyperspectral aircraft imagery converted to relative reflectance and dense coincident surface observations. This study is part of an effort to develop simple proxies for turbidity and algal blooms and to evaluate their performance and portability between satellite imagers for regional operational turbidity and algal bloom monitoring. Turbidity algorithms were then applied to synthetic satellite images and compared to in situ measurements of turbidity, chlorophyll-a (Chl-a), total suspended solids (TSS) and phycocyanin as an indicator of cyanobacterial/blue green algal (BGA) abundance. Several turbidity algorithms worked well with real Compact Airborne Spectrographic Imager (CASI) and synthetic WorldView-2, Sentinel-2 and Sentinel-3/MERIS/OLCI imagery. A simple red band algorithm for MODIS imagery and a new fluorescence line height algorithm for Landsat-8 imagery had limited performance with regard to turbidity estimation. Blue-Green Algae/Phycocyanin (BGA/PC) and Chl-a algorithms were the most widely applicable algorithms for turbidity estimation because strong co-variance of turbidity, TSS, Chl-a, and BGA made them mutual proxies in this experiment.

© 2018 International Association for Great Lakes Research. Published by Elsevier B.V. All rights reserved.

Introduction

Background

Algal blooms consisting of primarily photosynthetic phytoplankton, sometimes including blue-green algal (cyanobacterial) blooms and especially toxic or "harmful" algal blooms (HABs including CyanoHABs), are impacting numerous inland lakes and reservoirs world-wide (Heisler et al., 2008; Kudela and Gobler, 2012; Kudela et al., 2015a, b;

Lopez et al., 2008; Matthews and Bernard, 2013; USEPA, 2012; Wells et al., 2015). In this particular experiment, cyanobacteria dominated the phytoplankton population so our "HAB" was what has been more recently referred to as a "CyanoHAB". Many of these lakes and reservoirs are used as sources of drinking water (Graham, 2006; Linkov et al., 2009; Spear, 2014). Given that HABs (including CyanoHABs) are common and expected to increase in the future (Kudela et al., 2015a, b; O'Neil et al., 2012; Paerl and Paul, 2012) the development of satellite reflectance algorithms for economical and routine estimation of cyanobacterial (a.k.a blue-green algae or BGA) biomass has been a high research priority and has resulted in many effective algorithms for several satellite and aircraft imagers (Beck et al., 2016, 2017;

* Corresponding author.

E-mail address: richard.beck@uc.edu (R. Beck).

Binding et al., 2013; Gower et al., 2004, 2008; Kudela et al., 2015a, b; Mishra et al., 2009; Simis et al., 2005, 2007; Stumpf, 2014; Stumpf et al., 2012, 2016; Wynne et al., 2008, 2010, 2013;).

Regional and global early watch, warning and monitoring systems for HABs (including CyanoHABs) face a number of challenges including, a limited number of satellites appropriate for Chl-a and BGA monitoring in water and cloud cover in temperate climates, both of which limit revisit frequency (temporal resolution), and resource and logistical constraints for field sample collection and analysis. Although MERIS/OLCI is a good start for large water bodies, a “top-down” approach with a single universally applicable image product from a single satellite for global HAB monitoring is unlikely to work due to cloud cover, a variety of water constituent interactions, factors related to bathymetry, among others. This is especially true for smaller water bodies, including the bays and tributaries of larger lakes, some of which vary greatly in size over annual weather cycles. Similarly, a “bottom-up” approach in which all satellite data processing, field calibration and validation are done at the local level will be difficult to provide and maintain in many areas including in the developing world due to bandwidth, logistical and resource constraints.

A large number of well-established algorithms for HAB (including CyanoHAB) detection from a variety of inland water bodies have been reported in the peer-reviewed literature. Therefore, a hybrid approach that offers a limited variety of pre-computed standard image products available via local open source software or web GIS systems coupled with a simplified set of coincident surface observations such as water color and a turbidity measurement may be adequate for qualitative, “red flag-type”, early watch and warning systems for algal blooms. One might imagine organizations such as the European Space Agency (ESA), National Aeronautics and Space Administration (NASA), United States Geological Survey (USGS), National Oceanic and Atmospheric Administration (NOAA) or United States Army Corps of Engineers (USACE) generating 3 to 5 standard HAB image products per satellite and maintaining a citizen science web site that harvests latitude, longitude, water color and turbidity measurements. Water color could be limited to a structured vocabulary such as red, brown, green, blue, blue-green or clear. If the field data record is “green” or “blue-green” plus a high turbidity value it would be included in the calibration and validation data set for images of algal bloom severity.

Data mining methods leveraging open source software such as R could then quickly determine which standard HAB image products from a meta-constellation of available satellites (Sentinel-2A, -2B, Sentinel-3, Landsat-8 etc.) are most appropriate for each state (i.e. Ohio Environmental Protection Agency (EPA)) or region (i.e. Ohio River Valley Water Sanitation Commission (ORSANCO)) and revise their calibration and validation on the fly before classifying the images by turbidity values for publication in web GIS systems (Johansen et al., 2018). The interpretation of turbidity in terms of algal bloom severity (low, medium, high, severe) would be left to local and regional water quality managers who have the most detailed water quality expertise. Such professional or citizen science HAB monitoring systems could provide low-cost early watch (conditions make HABs including CyanoHABs more likely) and warning (cyanobacterial blooms have been detected) for drinking water sources and help focus limited and expensive sampling and analytical resources for the determination of toxicity.

Turbidity-, Chl-a-, and BGA/phycocyanin-based remote sensing-based warning systems should be initially limited to government water quality risk managers with the knowledge and resources to send out boats with water sampling crews to determine if toxicity exists, before making such warnings public. This caution is warranted because not all “algal blooms” produce toxins and those that can may or may not do so always (Stumpf et al., 2016). In combination with a second parameter such as water color (“green” or “blue-green”) it may be possible to achieve a useful working approximation at minimum cost with local to regional extensibility. Such a local to regional in situ turbidity proxy (approximation) for in situ BGA would be similar to the in situ

turbidity proxy for in situ Chl-a approximation developed by the USGS for lake monitoring with Landsat-7 for the state of Michigan (Fuller et al., 2004). Therefore we explore the relationship of remotely sensed turbidity to in situ turbidity (measured here with an optical probe rather than with a Secchi disk) and later to an in situ BGA/PC (cells/mL and Relative Fluorescence Units (RFU)) probe and laboratory chlorophyll measurements determined from 321 imager/algorithm combinations for five current satellite systems and one aircraft imaging system. The end goal of this study was to further the progress toward a local, regional and perhaps global first cut “red flag” warning system for HABs (including CyanoHABs) after some local or regional calibration and validation.

Turbidity as a proxy for HABs (including CyanoHABs) in highly productive green and blue-green turbid freshwaters

Algorithms for satellite imagers such as MERIS/OLCI that include the 620 nm phycocyanin absorption feature are more specific to cyanobacterial blooms and tend to have high accuracies (Binding et al., 2013; Stumpf et al., 2012, 2016). However, the large 300 m pixel size for MERIS/OLCI makes it difficult to apply to smaller water bodies including the bays associated with the Great Lakes as well as tributaries, smaller lakes and reservoirs in their watersheds. Such coarse imagery also masks the significant spatial heterogeneity that can be associated with HABs (including CyanoHABs), making precise spatial coordination of coincident surface observations to their large pixels challenging in the field. Recent experiments with aircraft hyperspectral imagery initiated on Lake Erie (Beck et al., 2011), and refined on smaller inland reservoirs in Ohio with easier sampling logistics (Beck et al. 2016, 2017) have enabled the synthesis of “coincident” synthetic satellite data for several satellite imagers with a range of pixel sizes and spectral resolutions (band or channel widths). These efforts have helped to identify promising families of algorithms that are portable across a range of spatial and spectral resolutions for HAB monitoring. Error budgets associated with the atmospheric correction of the real CASI hyperspectral aircraft data and with the construction of synthetic but isochronous approximations of real multispectral satellites were discussed in preceding Chl-a and BGA studies (Beck et al., 2016, 2017).

Space as a proxy for time

In this experiment we used dense surface water sampling of spatially varying water quality parameters during a snapshot in time with very high spatial as well as spectral resolution from the hyperspectral aircraft imager (Beck et al., 2016, 2017 and this paper) to substitute spatial variation for time in order to evaluate imager/algorithm combinations for Chl-a, BGA and turbidity (this paper) estimation. This space for time design has several advantages:

1. It avoids the common use of single time surface observations for the calibration and validation of image/algorithm combinations that are often days, weeks or months and sometimes years before or after the surface observations (Duan et al., 2012; Feng et al., 2015; Qi et al., 2015b).
2. It avoids the need to use temporal averaging of surface observations to calibrate and validate single aircraft or satellite overpasses (Qi et al., 2015a). These temporal averages conflate temporal variation of sun angle, atmospheric humidity and dust, air and water temperatures, wind orientations and speeds, wave orientations, wave heights, water quality constituents (Chl-a, BGA, turbidity, etc.) (Duan et al., 2012; Feng et al., 2015; Lee et al., 2010; Qi et al., 2015b) other than those being evaluated for various imager/algorithm combinations and sometimes even significant changes in water depth in the case of shallow waters subject to high winds and seiches such as Lake Taihu (Zhang, 1992) or Lake Erie. These temporal conflation problems are especially severe with highly

- dynamic water quality phenomena associated with phytoplankton where physiology and/or changes in wind speed can change the spectral signature of the water surface on the scale of hours (Hu et al., 2010). For example some of the data sets used for snapshot calibration show seasonal groupings (Qi et al., 2015a).
3. It avoids the need to use surface observations collected at different times in different parts of lakes (it avoids spatio-temporal conflation) for calibration and validation (Feng et al., 2015; Qi et al., 2015b).
 4. It nullifies the common use of a few point samples to calibrate and validate large satellite image pixels (Qi et al., 2014).
 5. Its higher spatial sampling density is a better match for higher resolution aircraft based hyperspectral or multispectral imagery.
 6. It does not mix and match different types of analyses for the same water quality parameter. For example some studies use laboratory analyses for the calibration and probe data for the validation of water quality algorithms (Qi et al., 2015a).
 7. It relies on real calibrated aircraft imagery (Brezonik et al., 2005; Han and Jordan, 2005; Kallio, 2000; Lillesand et al., 1983; Torbick et al., 2008; Zhang and Han, 2015) rather than water surface remote sensing reflectance (Rrs). Rrs often fails to predict aircraft or satellite algorithm performance (Feng et al., 2015; Qi et al., 2014; Qi et al., 2015a; Qi et al., 2015b) leading to the need to omit results for parts of lakes or even entire lakes (Feng et al., 2015).
 8. It uses optical probe data with corroborating laboratory analyses conducted according to standard protocols.
 9. It uses microscopic biological validation of phytoplankton taxa.
 10. It minimizes instrument drift in both the imagers and surface measurements when sampled over time.

Conflation of surface observations collected at different times often requires complex algorithms to obtain a good curve fit for the mixture of temporally dispersed data points (Feng et al., 2015; Qi et al., 2015b), the glossing over, or omission of statistics for the surface observations (Hu et al., 2015; Qi et al., 2015a;), the omission of surface observation maps (Hu et al., 2010) the use of log-log plots of algorithm indices vs. surface observations (Duan et al., 2012), the omission of results for lakes for which algorithms performed poorly (Qi et al., 2015b) or some combination of the above. These multi-temporal calibrations and validations are then often applied to snapshot aircraft or satellite images for the estimation of various water quality parameters with varying degrees of success (Feng et al., 2015).

As was shown in Beck et al. (2016, 2017) and below, our near elimination of most of the time-varying environmental and atmospheric variables reveals that the timing, type, quality and quantity of coincident surface observations are at least as important as the choice of algorithm or choice of atmospheric correction method used to process several types of hyperspectral and multispectral image data for the estimation of Chl-a, BGA, and in this study, turbidity. In reality, the elegant and scientifically sound "snapshot" method presented here and the more common multi-temporal conflation method for calibration and validation are complimentary. The snapshot coincident surface observation method is appropriate for the calibration and validation of snapshot imagery. The multi-temporal conflation surface observation method may be appropriate for the calibration and validation of averaged time-series imagery for annual summaries (Shi et al., 2017) or similar.

The space for time experiment suggested that several simple, semi-analytical (spectrally based) algorithms for chlorophyll-a (Chl-a) and phycocyanin (PC) will be adequate for use with several satellite imagers for tributary water bodies in the watersheds of Great Lakes as well as their smaller bays (Beck et al., 2016, 2017). These simple algorithms are extended in this paper to include turbidity to map algal blooms as part of a general first-cut "red flag" capability that leverages multiple satellite imagers, and to avoid the cloud cover issues associated with temperate climates.

Turbidity and related algorithm selection

Semi-analytical satellite reflectance algorithms that measure the depth and or width of the relatively narrow and shallow 620 nm feature associated with the phycocyanin (PC) pigment in BGA are the most specific to CyanoHABs (Kudela et al., 2015a, b; Simis et al., 2005). Most existing operational multispectral satellites are not capable of sensing the 620 nm phycocyanin absorption feature directly due to their relatively wide bands and traditional focus on the chlorophyll-a "veg edge" signature for both land and aquatic vegetation.

Therefore, the second most specific group of semi-analytical satellite reflectance algorithms for BGA estimation are the chlorophyll-a (Chl-a) algorithms (Augusto-Silva et al., 2014; Gower et al., 2004, 2008; Mishra et al., 2009; Mishra and Mishra, 2012; Wynne et al., 2008, 2012). Chl-a algorithms are popular for BGA estimation because they can be applied in combination with most existing operational multispectral satellite imaging systems (Augusto-Silva et al., 2014; Beck et al., 2016; Mishra et al., 2009; Mishra and Mishra, 2012). In some highly productive inland waters turbidity may also be an adequate predictor of algal bloom intensity as will be shown below.

Turbidity is a measure of relative clarity of a liquid (U.S. Geological Survey, 2015a, b). For remote sensing purposes, turbidity has been defined as "the concentration, size, shape and refractive index of suspended particles (that) determine turbidity and increase the amount of energy backscattered by water bodies" (Moore, 1980). The spectral signature of turbid water is variable accordingly. In practice most turbidity algorithms consider reflectance in the visible red wavelengths because this signal is from the upper 1 m of the water column and is proportional to the concentration of suspended reddish inorganic sediment (Moore, 1980; Stumpf and Pennock, 1989; Doxaran et al., 2002, 2006; Barnes et al., 2015) in the absence of aquatic vegetation.

Use of visible red reflectance values in turbidity algorithms also reduces the influence of the Chl-a NIR and green reflectance peaks somewhat (Olmanson et al., 2013) with modest aquatic vegetation and phytoplankton concentrations. High aquatic vegetation and phytoplankton concentrations result in strong absorption of red wavelengths and complicate the use of red band turbidity algorithms (Papoutsas et al., 2013). Other parts of the reflectance spectrum may be compared with the red reflectance values depending on the suspended and dissolved constituents contributing to the turbidity (Barnes et al., 2015; Dogliotti et al., 2015; Doxaran et al., 2002, 2006; Nechad et al., 2010.). Red reflectance values are often compared to green reflectance values (Doxaran et al., 2006) or NIR reflectance values (Dogliotti et al., 2015) depending on the water body under study. This complexity makes turbidity algorithms the third most specific group of semi-analytical (spectral signature based) satellite reflectance algorithms for BGA estimation.

The inorganic red sediment reflectance signature is relatively easy to sense directly in the absence of other spectrally active substances but difficult to interpret due to varying reflectance contributions from chlorophyll, phycocyanin, CDOM, tripton and other spectrally active substances in water with abundant phytoplankton and/or suspended sediment (Doxaran et al., 2002; Nechad et al., 2010; Simis et al., 2005, 2007). The amalgamated, and, therefore, spatially and temporally variable nature of turbidity requires at least some local empirical calibration to relate it to other water quality parameters such as Chl-a, phycocyanin, BGA, CDOM and suspended sediment (Figs. 1 and 2).

The dense cyanobacteria cells of CyanoHABs contribute strongly to the amalgamated turbidity reflectance signature. Therefore, while turbidity algorithms are less specific indicators of harmful and other algal blooms than phycocyanin and Chl-a algorithms, they are easier to adapt to existing satellite imaging systems with relatively broad bands such as Landsat-8 and MODIS.

Several studies have used high spectral resolution surface point and imaging spectroradiometers with numerous and narrow ("hyperspectral") band configurations to collect reflectance signatures of turbid inland waters in order to formulate algorithms to

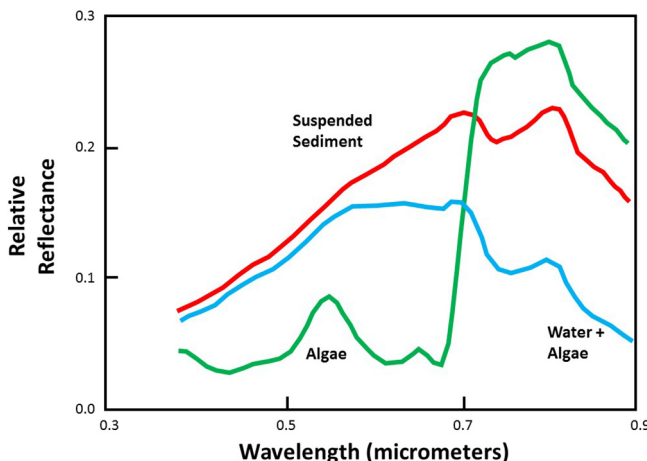


Fig. 1. Conceptual model with two extreme endmembers (high concentration of suspended inorganic red sediment and very high concentration of algae) and a mixture of water and algae for turbidity reflectance signatures in water from Jupp et al. (1994). X-axis is wavelength in microns. Y-axis is percent relative reflectance. (For interpretation of the references to color in this figure legend, the reader is referred to the web version of this article.)

estimate turbidity based on the turbidity reflectance signature (Doxaran et al., 2002; Kallio et al., 2001; Olmanson et al., 2013; Santini et al., 2010; Wu et al., 2014). The overarching goal of this study is to maximize temporal coverage for inland reservoirs for algal bloom detection by leveraging existing and near-future (at the time of the experiment) multispectral satellite imaging systems and by identifying the most “portable” turbidity and other BGA related water quality parameter index algorithms (Augusto-Silva et al., 2014; Mishra and Mishra, 2012; Shen et al., 2012). By “portable” we mean algorithms that work reasonably well (Pearson's r^2 equal to or >0.6) across different imagers and water bodies in the future. The option of using multiple satellites to image algal blooms in inland waters is especially important in humid, temperate climates where intermittent cloud cover limits temporal resolution for an individual satellite (Verbyla, 1995). Therefore, this research is focused on comparing relatively simple, and, therefore, portable, semi-analytical, and reflectance-signature-based algorithms that provide reasonable estimates of turbidity and/or phytoplankton biomass with current and near-future multispectral satellite imagers. The ultimate goal of this research is to explore and expand remote sensing-based options that could be used for near-real-time monitoring of inland water quality

(Binding et al., 2013; Dekker 1993; Fraser, 1998; Gitelson et al., 1993; Glasgow et al., 2004; Reif, 2011).

Study area

The Ohio River Watershed and its tributaries, often including reservoirs, are the sources of drinking water for $>5,000,000$ people (Vicory, 2009). The reservoirs are the sites of frequent algal blooms (including HABs and especially of CyanoHABs). The quality of water in the Ohio River is routinely monitored by the Ohio River Valley Water Sanitation Commission (ORSANCO), USEPA, Ohio EPA, and USGS. The water levels in the Ohio and the East Fork of the Little Miami Rivers (in which this case study occurs) are monitored by the USACE and USGS. NOAA monitors meteorological variables at nearby Lunken Airport in eastern Cincinnati. Harsha Lake lies within the East Fork of the Little Miami River Watershed above its confluence with the Little Miami River, which then flows into the Ohio River (Fig. 3). Harsha Lake is a compact 8.9 km^2 reservoir with simple logistics relative to the Great Lakes that enable the collection of dense coincident surface observations (CSOs). Most of the lake is deeper ($>5 \text{ m}$) than common Secchi disk depths ($<2 \text{ m}$). Therefore measured surface, aircraft and spacecraft spectra are due to water column, water surface and atmospheric phenomena rather than the bottom of the lake.

The East Fork Watershed and Harsha Lake is the subject of a long-term, routine non-point water quality study conducted by the USEPA in partnership with the USACE, Ohio EPA, and local water resource and conservation district professionals as part of the East Fork Little Miami River Watershed Cooperative (EFWCoop). In addition to being a source of drinking water, Harsha Lake has two public swimming beaches, hosts open water swimming and rowing events, and is used extensively for recreational fishing. When combined with water quality information resources, Harsha Lake becomes an excellent case study for several research issues related to HABs and CyanoHABs (Fig. 3).

We built upon the ongoing work of the multi-agency East Fork Watershed Cooperative (EFWCoop) to accurately quantify algal communities and coincident water physio-chemistries in Harsha Lake by establishing a partnership with the USACE Joint Airborne Lidar Bathymetry Technical Center of Expertise (JALBTCX) that supported an airborne survey using an Itres, Inc. Compact Airborne Spectrographic Imager (CASI)-1500 VNIR hyperspectral imager (HSI) mounted on a light aircraft. Research boats operated by the USACE, USEPA, Kentucky Division of Water and University of Cincinnati collected water quality and cyanobacterial data below the path of the aircraft within 1 h of image acquisition.

Methods

Hyperspectral imaging data consist of many sensitive, narrow bands spanning a wide spectral range, which allows for simultaneous retrieval of Chl-a, BGA/PC, TSS, turbidity, CDOM and other water quality parameters in coastal and lake waters (Koponen et al., 2002; Giardino et al., 2007). In order to accurately map and quantify algal blooms in general, including cyanobacterial blooms, we created a data set consisting of high spatial resolution (1 m ground sample distance (GSD)) with high spectral resolution, 14 nm full width half maximum (14 nm FWHM) airborne hyperspectral images with dense coincident surface observations, as an indirect proxy for BGA concentrations in order to be able to use the widest variety of satellite imagers. Details of the aerial survey and in situ measurement/sample collection are available in Beck et al. (2016, 2017).

This study of turbidity algorithms complements studies of Chl-a and phycocyanin algorithms for BGA estimation (Beck et al., 2016 and 2017) from the same data set. For all three studies, airborne hyperspectral imagery of our case study lake was upscaled to high and moderate resolution satellite imagery to develop specifications for a prototype multi-satellite monitoring system for HABs (including CyanoHABs). Details

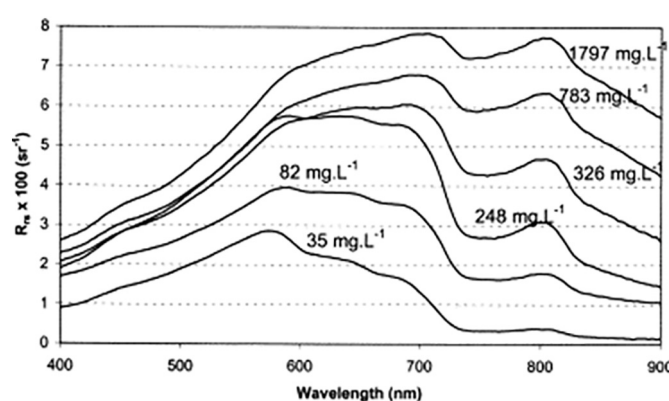


Fig. 2. Averaged spectra measured above turbid water over visible and near-infrared (NIR) wavelengths at varying inorganic red sediment concentrations (from Doxaran et al., 2002). X-axis is wavelength in nanometers. Y-axis is calibrated remote sensing reflectance (Rs).

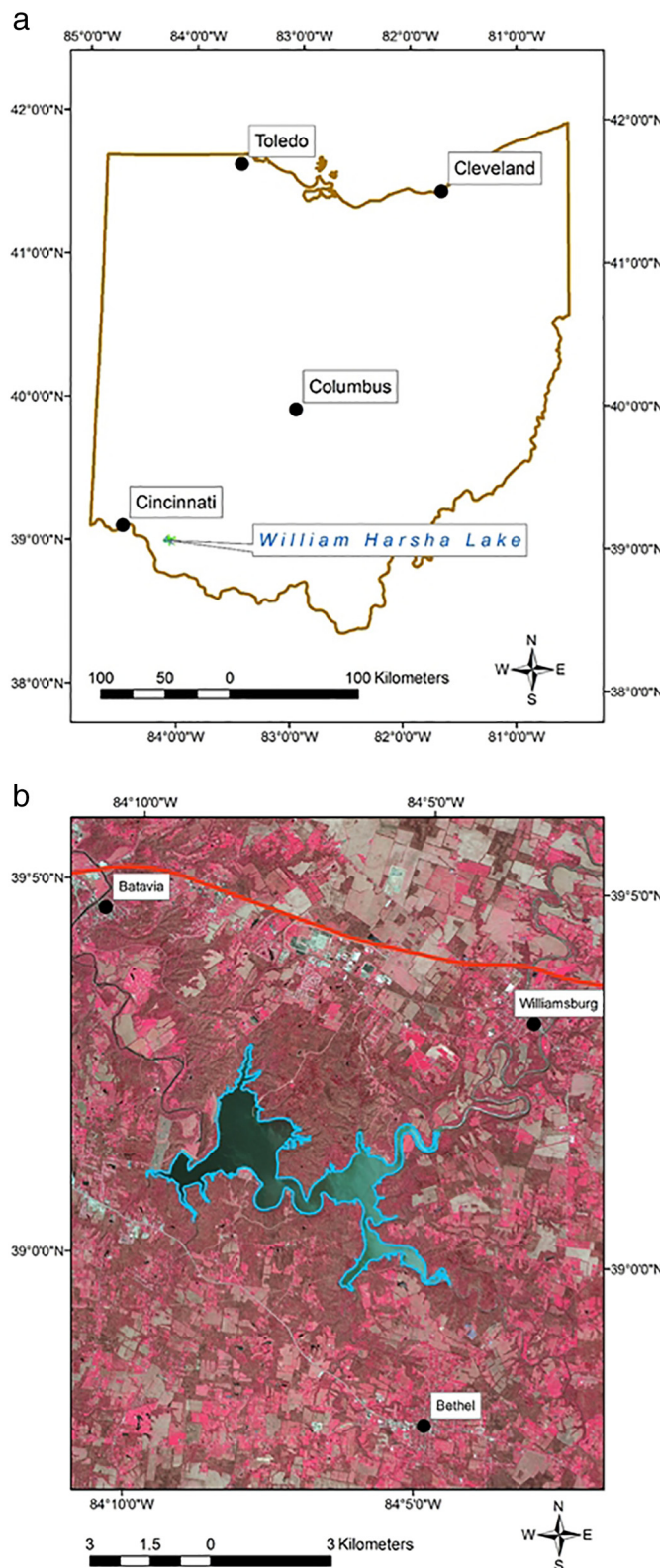


Fig. 3. Location maps of Harsha (East Fork) Lake near Cincinnati, Ohio. Location in Ohio (3a) and in detail (3b).

of the synthetic satellite image construction are available in Beck et al. (2016, 2017).

Several satellite reflectance algorithms for estimating turbidity in water have been developed (Bowers and Binding, 2006; Chipman et al., 2009; Dogliotti et al., 2015; Doxaran et al., 2002; Guttler et al.,

2013; Harrington et al., 1992; Lathrop et al., 1991; Moore, 1980; Nechad et al., 2010; Potes et al., 2012; Ruddick et al., 2008; Shen et al., 2012; Wu et al., 2014). Given our goal of finding relatively simple, semi-analytical, turbidity reflectance algorithms that are easily adapted to a variety of satellite imagers, we have summarized the available bands by imager in Table 1 and candidate algorithms and their authors in Table 2 and 321 variants adapted to 5 satellites in Electronic Supplementary Material (ESM) Table S1

Data sets

Our research used the following key data sets: airborne visible and near-infrared (VNIR) hyperspectral imagery of Harsha Lake and extensive, coincident surface spectral observations (Fig. 4) consisting of laboratory measurements of water quality parameters and in situ water sensors. These data sets were used to develop and/or evaluate and

Table 1

Band wavelength ranges, centers and widths for original and synthetic satellite imagers (Beck et al., 2016). FWHM is Full Width Half Maximum.

Imager	Original range (nm)	Center (nm)	FWHM (nm)	Synthetic range (nm)	Synthetic center (nm)	FWHM (nm)
Resampled to 1.8 m						
WorldView-2/3						
b1	400–450	425	50	403–454	428.5	51
b2	450–510	480	60	454–505	479.5	51
b3	510–580	545	70	523–573	548	50
b4	585–625	605	40	582–633	607.5	51
b5	630–690	660	60	634–684	659	50
b6	705–745	725	40	710–749	729.5	39
b7	770–895	832.5	125	790–889	839.5	99
b8	860–1040	950	180	889–1043	966	154
Resampled to 20 m						
Sentinel-2						
b1	433–453					
b2	458–523	490.5	65	457–515	486	58
b3	543–578	560.5	35	543–572	557.5	29
b4	650–680	665	30	643–686	664.5	43
b5	698–713	705.5	15	700–714	707	14
b6	733–748	740.5	15	728–743	735.5	15
b7	773–793	783	20	771–800	785.5	29
b8	785–900	842.5	115	785–900	842.5	115
b8b	855–875	865	20	856–871	863.5	15
b9	935–955	945	20	935–955	945	20
Resampled to 30 m						
Landsat-8						
b1	430–450	440	20	429–443	436	14
b2	450–510	480	60	457–500	478.5	43
b3	530–590	560	60	529–586	557.5	57
b4	640–670	655	30	643–672	657.5	29
b5	850–880	865	30	856–885	870.5	29
Resampled to 250 m						
MODIS						
b1	620–670	645	50	615–672	643.5	57
b2	841–876	858.5	35	842–871	856.5	29
Resampled to 300 m						
MERIS/OLCI						
b1	402–412	407	10	400–414	407	14
b2	438–448	443	10	429–457	443	28
b3	485–495	490	10	486–500	493	14
b4	505–515	510	10	500–515	507.5	15
b5	555–565	560	10	558–572	565	14
b6	615–625	620	10	615–629	622	14
b7	660–670	665	10	657–672	664.5	15
b8	678–685	681.5	7	672–686	679	14
b9	704–714	709	10	700–714	707	14
b10	750–757	753.5	7	743–757	750	14
b11	757–762	759.5	5	750–764	757	14
b12	772–787	779.5	15	757–800	778.5	43
b13	855–875	865	20	842–885	863.5	43
b14	880–890	885	10	871–899	885	28
b15	895–905	900	10	885–913	899	28

Table 2

Band math and original specified wavelengths in nm for each algorithm used for turbidity estimation at Harsha Lake. Algorithms with asterisk measure the 620 nm phycocyanin absorption feature directly while those with "Turb" designation were published as turbidity algorithms. The remaining algorithms were originally published as chlorophyll-a and phycocyanin algorithms. Asterisk denotes design for phycocyanin. Float refers to floating point values of relative reflectance in the ENVI band math we used in this study for each band at the specified wavelengths in nm from atmospherically corrected imagery. Float is not a variable, it is an IDL function used to prevent byte overflow errors during calculation.

Algorithm	Reference	Band math with original specified wavelengths (Numerical value = wavelength in nm)
AI10SABI	Alawadi (2010)	$(\text{float}(857)-\text{float}(644))/(\text{float}(458) + \text{float}(529))$
Am092Bsub	Amin et al. (2009)	$(\text{float}(681))-(\text{float}(665))$
Am09KBBI	Amin et al. (2009)	$(\text{float}(686)-\text{float}(658))/(\text{float}(686) + \text{float}(658))$
Be162Bdiv	This paper	$(\text{float}(681))/(\text{float}(665))$
Be162Bsub*	This paper	$(\text{float}(700))-(\text{float}(622))$
Be16FLHblue	Beck et al. (2016)	$(\text{float}(529))-\text{float}((\text{float}(644) + (\text{float}(458)-\text{float}(644)))$
Be16FLHPhy*	This paper	$(\text{float}(620))-\text{float}((\text{float}(709) + (\text{float}(560)-\text{float}(709)))$
Be16FLHViolet	Beck et al. (2016)	$(\text{float}(529))-\text{float}((\text{float}(644) + (\text{float}(5)-\text{float}(644)))$
Be16NDPhyl*	This paper	$(\text{float}(700))-(\text{float}(622))$
DE933BDA	Dekker (1993)	$((\text{float}(600))-\text{float}(648))-(\text{float}(625))$
Gi033BDA	Gitelson et al. (2003)	$((1/\text{float}(672))-(1/\text{float}(715)))*(\text{float}(757))$
Go04MCI	Gower et al. (2004)	$((\text{float}(709))-(\text{float}(681))-(\text{float}(753))-(\text{float}(681))))$
HU103BDA*	Hunter et al. (2008)	$((1/\text{float}(615))-(1/\text{float}(600)))-(\text{float}(725))$
Kn07KIVU	Kneubuhler et al. (2007)	$(\text{float}(458)-\text{float}(644))/(\text{float}(529))$
Ku15PhyCl	Kudela et al. (2015a, b)	$\text{neg}^*((\text{float}(681))-(\text{float}(665))-(\text{float}(709))-(\text{float}(665))))$
MI092BDA	Mishra et al. (2009)	$(\text{float}(700))/\text{float}(600)$
MM092BDA	Mishra et al. (2009)	$(\text{float}(724))/\text{float}(600)$
MM12NDCI	Mishra and Mishra (2012)	$(\text{float}(700)-\text{float}(665))/(\text{float}(700) + \text{float}(665))$
MM143BDAAopt*	Mishra and Mishra (2014)	$((1/\text{float}(629))-(1/\text{float}(659)))*(\text{float}(724))$
MM143BDAAver3merisver*	Mishra and Mishra (2014)	$((1/\text{float}(620))-(1/\text{float}(665)))*(\text{float}(778))$
SI052BDA*	Simis et al. (2005)	$(\text{float}(709))/\text{float}(620)$
SM122BDA	S. Mishra (2012)	$(\text{float}(709))/\text{float}(600)$
SY002BDA*	Schalles and Yacobi (2000)	$(\text{float}(650))/\text{float}(625)$
Be16NDTblue	This paper.	$(\text{float}(658)-\text{float}(458))/(\text{float}(658) + \text{float}(458))$

Table 2 (continued)

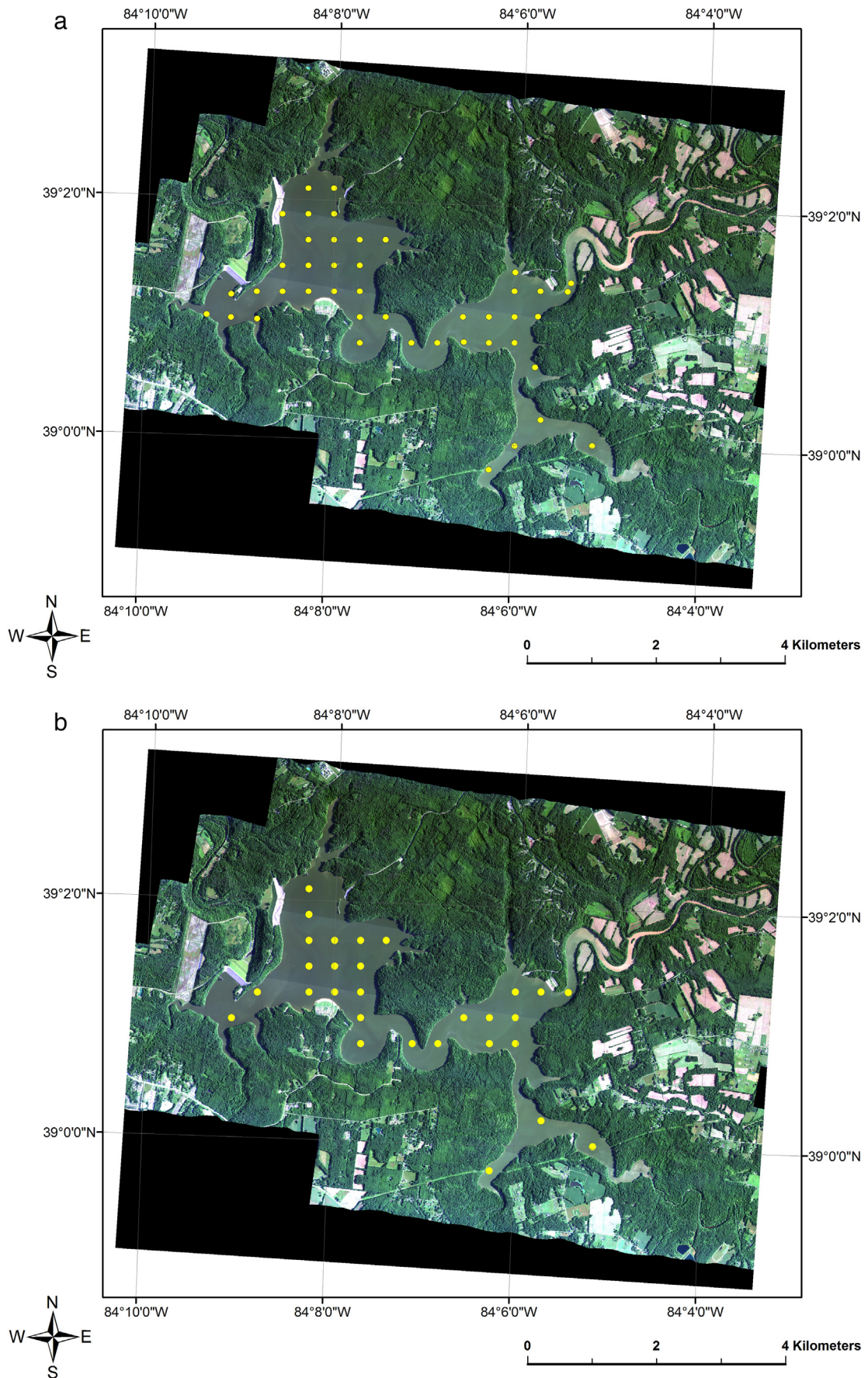
Algorithm	Reference	Band math with original specified wavelengths (Numerical value = wavelength in nm)
Be16NDTblue	This paper.	$\text{float}(458))$ $(\text{float}(658)-\text{float}(444))/(\text{float}(658) + \text{float}(444))$ $(\text{float}(658))-\text{float}((\text{float}(857) + (\text{float}(458)-\text{float}(857)))]$ $(\text{float}(658))-\text{float}((\text{float}(857) + (\text{float}(558)-\text{float}(857)))]$ $(\text{float}(658))-\text{float}((\text{float}(857) + (\text{float}(444)-\text{float}(857)))]$
Be16FLHBlueRedNIR	This paper.	$((\text{float}(558)) + (\text{float}(658)))/(\text{float}(444))$ $(\text{float}(658))/(\text{float}(444))$
Be16FLHGreenRedNIR	This paper.	$+ (\text{float}(558)-\text{float}(857))]$ $(\text{float}(658))-\text{float}((\text{float}(857) + (\text{float}(558)-\text{float}(857)))]$
Be16FLHVioletRedNIR	This paper.	$+ (\text{float}(444)-\text{float}(857))]$
TurbBe16GreenPlusRedBothOverViolet	This paper.	$((\text{float}(558)) + (\text{float}(658)))/(\text{float}(444))$
TurbBe16RedOverViolet	This paper.	$(\text{float}(658))/(\text{float}(444))$
TurbBow06RedOverGreen	Bowers and Binding (2006)	$(\text{float}(658))/(\text{float}(558))$
TurbChip09NIROverGreen	Chipman et al. (2009)	$(\text{float}(857))/(\text{float}(558))$
TurbDox02NIRoverRed	Doxaran et al. (2002)	$(\text{float}(857))/(\text{float}(558))$
TurbFrohn09GreenPlusRedBothOverBlue	Frohn and Autrey (2009)	$((\text{float}(558)) + (\text{float}(658)))/(\text{float}(458))$
TurbHarr92NIR	Harrington (1992)	$(\text{float}(857))$
TurbLath91RedOverBlue	Lathrop et al. (1991)	$(\text{float}(658))/(\text{float}(458))$
TurbMoore80Red	Moore (1980)	$(\text{float}(658))$

calibrate a set of numerical algorithms for mapping the quantitative estimation of turbidity concentration.

Aircraft and field campaign

Details of our mission planning and field campaign at Harsha Lake are available in Beck et al. (2016). A temporal filtering process resulted in the acquisition of aircraft-based hyperspectral imagery and coincident surface observations on the morning of 27 June 2014. A Compact Airborne Spectrographic Imager (CASI)-1500 VNIR airborne hyperspectral imaging system was flown at an altitude of approximately 2000 m and acquired 48-band hyperspectral image strips 1466-meters wide at 1-meter spatial and 14 nm Full Width Half Maximum (FWHM) spectral resolution over a wavelength range of 371 to 1042 nm. Details of our hyperspectral image acquisition and pre-processing are also available in Beck et al. (2016). Tests with extracted water pixel Fast Line-of-sight Atmospheric Analysis of Hypercubes (FLAASH) reflectance spectra after atmospheric correction are similar to water field spectral measurements and display a turbidity spectral signature of amalgamated aquatic flora, water and suspended sediment. This study used wavelengths from 425 to 865 nm (Table 2) so we then created an observed vs. predicted (OP) (Analytical Spectral Devices (ASD) spectrometer vs. CASI) regression for all reflectance value pairs between those wavelengths (Fig. 5) (Beck et al., 2017). Details of the reflectance comparison are available in Beck et al. (2017).

We considered satellite/algorithm combinations that use proxy parameters such as turbidity (this paper) and Chl-a (Beck et al., 2016) in addition to those that sense phycocyanin and BGA directly (Beck et al., 2017). We included an extensive survey of water quality parameters



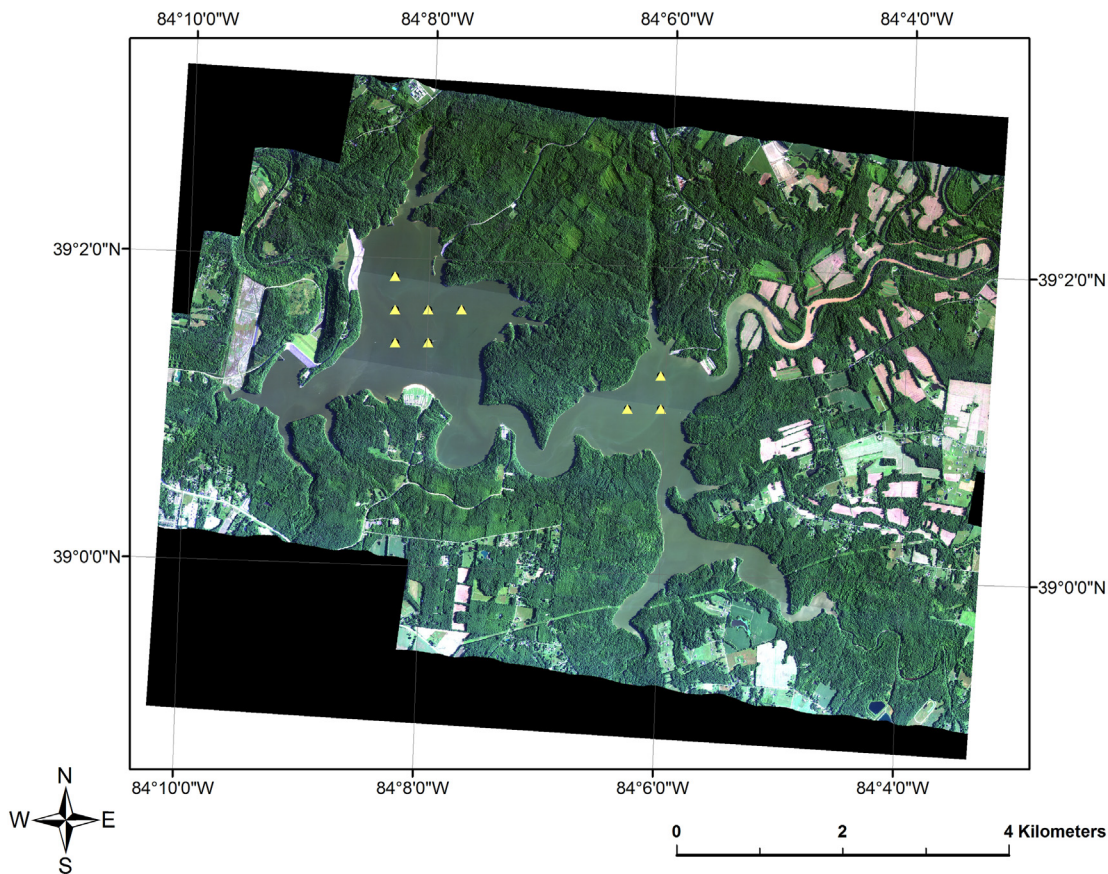


Fig. 4. Image of Harsha (East Fork) Lake acquired with a CASI-1500 image on 27 June 2014 with coincident surface observation (CSO) locations used in this study. We acquired 44 coincident water quality sonde and water samples within 1 h of image acquisition to evaluate the performance of 37 algorithms and 321 variants for estimating turbidity in a temperate reservoir for five satellite imaging systems. Fig. 4a shows the 44 CSO locations used to evaluate algorithms with real 1 m GSD CASI hyperspectral imagery. Fig. 4b shows the 27 CSO locations used to evaluate algorithms with synthetic WorldView-2, Landsat-8, and Sentinel-2 imagery. Fig. 4c shows the 9 CSO locations used to evaluate algorithms with synthetic MODIS and MERIS imagery.

in the lake at the time of acquisition in order to determine why some proxy indices such as turbidity (this study), Chl-a, and BGA/PC (Beck et al., 2016, 2017 and references therein) also work with regard to BGA estimation.

Coincident surface observation procedures

In order to compare the performance of turbidity algorithms with CASI aircraft and several synthetic multispectral satellite data sets, we deployed four research boats and acquired 44 coincident surface observations on a 400 m grid point spacing with cross-calibrated YSI water quality sondes on the same day within 1 h of CASI aircraft image acquisition. Surface observation collection was coordinated with the imaging aircraft via an air-to-ground radio.

Water samples collected at each of the ground truth sites were analyzed by the US EPA using standard methods for Total Organic Carbon (TOC (mg/L)), Dissolved Organic Carbon (DOC (mg/L)), Particulate Organic Carbon (POC (mg/L)), Total Phosphorus (TP ($\mu\text{gP/L}$)) Total Dissolved Phosphorus (TDP ($\mu\text{gP/L}$)); Particulate Phosphorus (PP ($\mu\text{gP/L}$)), Total Reactive Phosphorus (TRP ($\mu\text{gP/L}$)), Dissolved Reactive Phosphorus (DRP ($\mu\text{gP/L}$)), Particulate Reactive Phosphorus (PRP ($\mu\text{gP/L}$)), Total Nitrogen (TN ($\mu\text{gN/L}$)), Total Dissolved Nitrogen (TDN (μgNL)), Particulate Nitrogen (PN ($\mu\text{gN/L}$)), Dissolved Nitrite-Nitrate (DNO2-3 ($\mu\text{gN/L}$)), Total and Dissolved Ammonia (TNH4 and DNH4($\mu\text{gN/L}$, respectively)), Chlorophyll-a, turbidity, Total Suspended Solids (TSS (mg/L)), Volatile Suspended Solids (VSS (mg/L), % Suspended Organic Matter, Alkalinity (mg/L as CaCO_3) and Hardness (mg/L as CaCO_3). These additional water quality data were used to determine why

some proxy indices including some BGA and Chl-a algorithms also worked well for estimating turbidity in this experiment.

Synthetic satellite imagery

In order to have “coincident” imagery from several different satellite imagers paired with coincident surface observations, we extended the

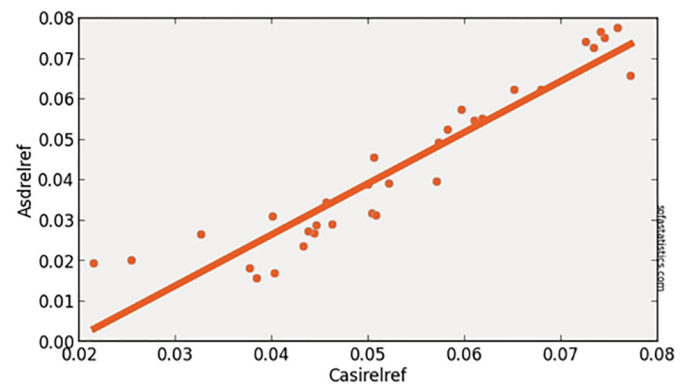


Fig. 5. Pearson's test of linear correlation for an averaged spectrum from 16 locations in the eastern basin of Harsha Lake from an Analytical Spectral Devices (ASD) surface spectroradiometer relative reflectance vs. an averaged spectrum from the same 16 locations from CASI (aircraft) relative reflectance values at 32 wavelengths ($n = 32$). $R^2 = 0.89$, $p < 0.001$, degrees of freedom = 30, slope = 1.265, intercept = -0.024. The in situ (lake) ASD spectra and the CASI spectra were acquired within 1 h of each other. Asdrefrel is ASD relative reflectance, Casirefrel is CASI relative reflectance, both measured against a Spectralon standard.

surface spectrometer work of [Augusto-Silva et al. \(2014\)](#) by binning high spatial resolution hyperspectral relative reflectance imagery with numerous narrow bands into artificial or “synthetic” broad band satellite imagery in order to approximate their relative performance with algorithms for the estimation of turbidity, Chl-a and BGA PC ([Beck et al., 2016, 2017](#)). Hyperspectral bands were spectrally averaged with equal weight using “Band Math” in ENVI to produce synthetic satellite image bands for Landsat-8, Sentinel-2/MSI, Sentinel-3/MERIS/OLCI, MODIS, and WorldView-2/3, according to published specifications ([DigitalGlobe, 2009, 2014](#); [European Space Agency \(ESA\), 2012, 2013](#); [Lindsey and Herring, 2001](#); [U.S. Geological Survey, 2015a, b](#)). Given our focus on smaller inland water bodies and the difficulties of relating very large pixels to discrete coincident surface observations, we have not simulated image data sets with bands with spatial resolutions coarser than 300 m. We used simple linear spectral binning of the CASI data to approximate all of the imagers because we did not know the post-launch spectral response of Sentinel-2, WorldView-3 or of the MERIS/OLCI follow on imagers at the time of this study as described in [Beck et al. \(2016\)](#). These synthetic bands were then resampled to the appropriate spatial resolution using “Resize Data” in ENVI. The resulting synthetic bands designations used in the subsequent analysis are shown in [Table 1](#). Error budgets associated with the construction of synthetic satellite multispectral imagery from real CASI hyperspectral relative reflectance imagery are discussed in [Beck et al. \(2016\)](#).

Image analysis

We extended the coincident surface synthetic sensor methodology of [Augusto-Silva et al. \(2014\)](#) to temperate inland reservoirs using aircraft acquired hyperspectral imagery ([Kallio, 2000](#); [Koponen et al., 2002](#); [Mittenzwey et al., 1992](#)) instead of surface based spectroradiometer data. Our aircraft imagery was also converted to relative reflectance at the surface and then artificially binned to create synthetic MERIS, MODIS, WorldView-2/-3, Sentinel-2 and Landsat-8 images ([Table 1](#)) that are “coincident” with a large coincident surface observation campaign as suggested by [Reif \(2011\)](#). We then applied 37 algorithms to create a performance ranked list of algorithm options by satellite imaging system for water resource managers concerned with inland water quality ([Chipman et al., 2009](#)). [Tables 2](#) and ESM Table S1 list the 37 image processing algorithms and their 321 abbreviations as used in this study by imaging system.

We used the Band Math function in ENVI 5.1 to apply 37 algorithms ([Table 2](#)) to the original CASI reflectance data to establish a performance base-line before creating synthetic imagery that corresponds to the band spacing of currently operational WorldView-2 and -3, Landsat-8, MODIS and near-future (at the time of the experiment) Sentinel-2 and Sentinel-3 (MERIS-like OLCI) satellite imaging systems ([Table 2](#)). Not all algorithms could be applied to all synthetic images due to band position, band spacing and band width constraints ([Cairns et al., 1997](#); [Lathrop and Lillesand, 1986](#)). We focused on 37 relatively simple reflectance-signature-based (semi-analytical) ratio and shape metric algorithms and their 321 variants adapted to five satellite imagers (ESM Table S1) for the sake of simplicity, brevity, portability between imagers and ease of application by water resource managers. We then evaluated their performance so that water resource managers may compare them against existing algorithms for the estimation of turbidity with satellite imagery.

Data analysis

We followed the example of [Kudela et al. \(2015a, b\)](#) and used a standard Type-1 linear regression test ([Pinero et al., 2008](#)) with twenty-nine points from water only pixels to compare the CASI and synthetic WorldView-2, Sentinel-2 and Landsat-8 imagery predictions on the X-axes to laboratory observations (measurements) of turbidity (Turbidity-NTU) on the Y-axes to avoid mixed pixels that included the shoreline

after rigorous quality control of coincident surface observations. Nine points were used to evaluate synthetic MODIS and MERIS imagery for the same reason. Measured turbidity (NTU) values were then compared to extracted image turbidity index point values at each location and their statistical relationship evaluated with Pearson's r (ESM Table S2). We then used a standard Type 1 regression test for the turbidity indices against measured turbidity values to normalize all results to the same units to facilitate comparison of the performance of each algorithm following the method of [Kudela et al. \(2015a, b\)](#) (ESM Table S3).

We used a critical *p*-value of 0.001 for all Pearson's r Type 1 regression tests. Some researchers ([Stumpf et al., 2016](#)) prefer Standard Error of Regression (Standard Error of Estimate or S) values to Type 1 (Pearson's) r^2 values so we have also included them for the top performing algorithms from ESM Table S3 for comparison ([Table 3](#)). Other researchers prefer Type 2 regressions ([Peltzer, 2015](#)) to test correlations of observed vs. predicted values in natural systems. Therefore, we also applied the Type 2 geometric mean method of Peltzer (2015) to turbidity estimation at Harsha (East Fork) Lake with all results again normalized to NTU turbidity values for top performing algorithms by Type 1 regression tests ([Kudela et al., 2015a, b](#)) ([Table 4](#)).

Single-band output from the Band Math function in ENVI for each turbidity algorithm (Band Math Field in [Tables 2](#) and ESM S1) was point sampled using the coincident surface observation locations to extract turbidity index (image) values for comparison with measured turbidity values (Turbidity-NTU) from water samples (ESM Table S2). All of the synthetic imagery used for the following performance analysis with regard to the estimation of turbidity are derived from VNIR CASI data atmospherically corrected to reflectance. Therefore, the following results (ESM Table S2) are for atmospherically corrected imagery for all of the synthetic sensors considered below. We applied a standard Type 1 regression test (Pearson's r) for the turbidity indices normalized to the same units (NTU) to facilitate comparison of the performance of each algorithm (ESM Table S3) following [Pinero et al. \(2008\)](#) and [Kudela et al. \(2015a, b\)](#) as described above. We used 0.001 as our critical *p* value. Algorithms are ranked with regard to their performance with regard to turbidity estimation in ESM Table S4.

Results

CASI imagery

We applied the algorithms listed in [Table 3](#) to the 1-meter, 48-band CASI VNIR hyperspectral reflectance image mosaic ([Tables 2, 3 and 4](#), ESM S, S2 and S3, [Fig. 6](#)). The performance of each algorithm in [Tables 2](#) and ESM S1 applied to the CASI reflectance imagery was then evaluated using 29 coincident surface observations for the sake of consistency with synthetic WorldView-2 and -3, Sentinel-2 and Landsat-8 imagery (other ≤ 30 m imagery). Simple subtraction and ratio-based algorithms suppress illumination variation well and had the best performance with regard to turbidity estimation. In decreasing order of performance (based on Pearson's r^2), the CASIBe16NDPhyl, CASIBe162B700sub601, CASISi052BDA, CASIMM12NDClalt, and CASIMM122BDA algorithms worked well (Pearson's $r^2 > 0.600$) for turbidity estimation with CASI imagery. Index imagery with raw and normalized index Type 1 (Pearson's r) linear regressions are shown for the best performing algorithm (CASIBe16NDPhyl) in [Fig. 6](#).

WorldView-2 (synthetic)

We applied 25 existing and 3 new algorithms to synthetic 1.8-meter, WorldView-2 imagery to examine the degree of portability of some of the simpler algorithms between (synthetic) satellite imaging systems ([Tables 2, 3, 4](#), ESM S1, S2 and S3, [Fig. 7](#)). In decreasing order of performance, the WV2Be162Bsub, WV2Si052BDA, WV2Be16NDPhyl, WV2Mi092BDA and WV2Am092Bsub algorithms had acceptable performance (Pearson's $r^2 > 0.600$) with this sensor

Table 3

Performance of Algorithms for turbidity estimation at Harsha (East Fork) Lake with all results normalized to calculated turbidity values with additional Type 1 Regression tests for Standard Error of Regression (Standard Error of Estimate or S values) and associated statistics.

Algorithms by satellite/sensor (with wavelengths)	R-Squared	Adj.R-Sqr.	Std.Err.Reg. S	Std. dev.	N	Residual mean square	p	Conf. level
CASIBe16NDPhyl (float(700)-float(601))/(float(700) + float(601))	0.639	0.626	1.603	2.621	29	2.568	<0.001	95.0%
WV2Be162Bsub (float(730))-float(608))	0.698	0.687	1.466	2.621	29	2.148	<0.001	95.0%
S2Si052BDA (float(707))/(float(665))	0.624	0.610	1.637	2.621	29	2.680	<0.001	95.0%
L8Be16FLHVioletRedNIR (float(530))-[float(640) + (float(430)-float(640))]	0.256	0.228	2.302	2.621	29	5.301	0.005	95.0%
MODISTurbMoore80Red (float(644))	0.394	0.307	1.575	1.892	9	2.479	0.070	95.0%
MERISTurbDox02NIRoverRed (float(864))/(float(665))	0.898	0.883	0.647	1.892	9	0.419	<0.001	95.0%

in this experiment (Fig. 7). The performance of each algorithm in Tables 2 and ESM S1 applied to the synthetic WorldView-2 imagery was evaluated using 29 coincident surface observations. As with CASI, simple subtraction and ratio-based algorithms suppress illumination variation well and had the best performance with regard to turbidity estimation. Index imagery with raw and normalized index Type 1 (Pearson's r) linear regressions are shown for the best performing turbidity algorithm (WV2Be162Bsub) in Fig. 7.

Sentinel-2 (synthetic)

We applied 23 existing and 3 new algorithms to the 20-meter, synthetic Sentinel-2 imagery. The performance of each algorithm in Tables 2 and ESM S1 applied to the synthetic Sentinel-2 imagery was evaluated using 29 coincident surface observations chosen to avoid pixels that mixed land and water at 20 and 30 m spatial resolutions (ESM Table S2). The S2Si052BDA, S2MM12NDCI and S2Be162Bsub algorithms had acceptable performance (Pearson's $r^2 > 0.600$) with this sensor in this experiment despite not being designed specifically for turbidity estimation. The S2Am2BsubTurb algorithm had only slightly lower performance. The S2Si052BDA, S2MM12NDCI and S2Be162Bsub algorithms also appear to have good portability between CASI, WorldView-2/-3 and Sentinel-2 imagery (Tables 2, 3, 4, ESM S1, S2 and S3, Fig. 8). Index imagery with raw and normalized index Type 1 (Pearson's r) linear regressions are shown for the best performing algorithm (S2Si052BDA) in Fig. 8.

Landsat-8 (synthetic)

We applied 21 existing and 3 new algorithms to the 30-meter, synthetic Landsat-8 imagery. None of the spectrally-oriented semi-analytical algorithms considered here had acceptable performance (Pearson's $r^2 > 0.600$) with regard to turbidity estimation with this sensor in this experiment. We formulated a new fluorescence line height (FLH) shape metric algorithm (Gower et al., 2004) to sense the red reflectance (L8Be16FLHVioletRedNIR) relative to the violet and NIR bands with modest success (Tables 2, 3, 4, ESM S1, S2 and S3, Fig. 9). The best performing algorithm was the new L8Be16FLHVioletRedNIR algorithm that incorporated the new ultra blue ("violet") coastal band for this sensor in this experiment. Index imagery with raw and normalized index Type 1 (Pearson's r) linear regressions are shown for the best performing algorithm (L8Be16FLHVioletRedNIR) in Fig. 9. Local empirical algorithms based on other water quality parameters such as turbidity with local calibration and validation are required for use with Landsat-8 for reliable turbidity estimation (Sun et al., 2015).

MODIS (synthetic)

We applied four existing algorithms (MODISMM12NDCI, MODISTurbDox02NIRoverRed, MODISTurbHarr92NIR and MODISTurbMoore80Red) to synthetic MODIS bands 1 and 2 (Lindsey and Herring, 2001) for turbidity estimation with limited success (Tables 2, 3, 4, ESM S1, S2 and S3, Fig. 10). The performance

Table 4

Performance of Algorithms for Turbidity (NTU) Estimation at Harsha (East Fork) Lake with all results normalized to calculated turbidity values with additional Type 2 Geometric Mean Tests (Peltzer, 2015) for top performing algorithms by Type 1 Regression tests (Kudela et al., 2015a, b). Float refers to floating point values of relative reflectance in the ENVI band math we used in this study at the specified wavelengths in nm from atmospherically corrected imagery. Float is not a variable, it is an IDL function used to prevent byte overflow errors during calculation.

Algorithms by satellite/sensor (with wavelengths)	Spatial Res. (m)	N	Geometric mean slope	Geometric mean intercept	Geometric mean correlation coefficient	Geometric mean correlation coefficient squared	Standard deviation of slope	Standard deviation of Y-intercept
CASIBe16NDPhyl (float(700)-float(601))/(float(700) + float(601))	1	29	1.251	-3.548	0.800	0.640	0.152	2.179
WV2Be162Bsub (float(730))-float(608))	1.8	29	1.186	-2.592	0.836	0.699	0.131	1.870
S2Si052BDA (float(707))/(float(665))	20	29	1.266	-3.768	0.790	0.624	0.158	2.260
L8Be16FLHVioletRedNIR (float(530))-[float(640) + (float(430)-float (640))]	30	29	1.986	-13.851	0.506	0.256	0.380	5.380
MODISTurbMoore80Red (float(644))	250	9	1.597	-8.102	0.628	0.394	0.521	7.128
MERISTurbDox02NIRoverRed (float(864))/(float(665))	300	9	1.055	-0.759	0.947	0.897	0.130	1.785

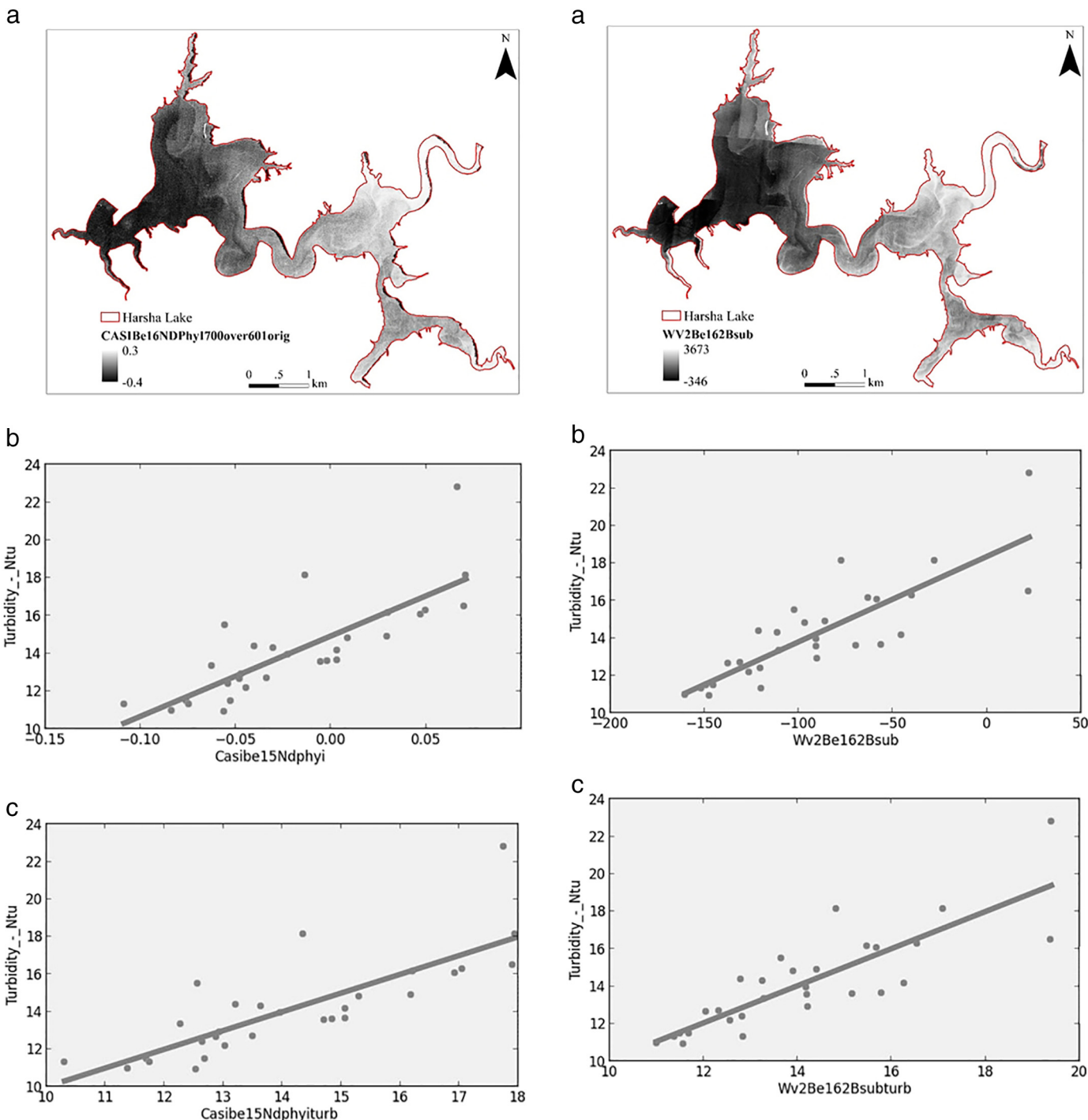


Fig. 6. Results of CASIBe16NDPhy1 algorithm as raw index values as applied to original CASI imagery with brighter pixels in the reservoir indicating higher turbidity (6a). Evaluation via observed (Y axis = Turbidity-NTU) vs. calculated raw CASIBe16NDPhy1 index value with Pearson's r^2 ($r^2 = 0.640$, $p < 0.001$, $N = 29$ to avoid shorelines) (6b). Evaluation via observed (Y axis = Turbidity-NTU) vs. calculated turbidity concentration (CASIBe16NDPhy1PHY) with Pearson's r^2 ($r^2 = 0.640$, $p < 0.001$, $N = 29$ to avoid shorelines) (6c). Details of the synthetic bands and band math are available in Tables 1, 2 and SI1 respectively.

of each algorithm in Tables 2 and S1 applied to the synthetic MODIS imagery was evaluated using nine coincident surface observations. These nine points were chosen to avoid pixels that mixed land and water at 250 and 300 m spatial resolutions (Fig. 4). MODIS bands 1 and 2 were simulated with the CASI data at 250 m spatial resolution to facilitate comparison of algorithm performance. MODIS bands 1 and 2 are

Fig. 7. Results of WV2Be162Bsub algorithm as raw index values as applied to synthetic WorldView imagery with brighter pixels in the reservoir indicating higher turbidity (7a). Evaluation via observed (Y axis = Turbidity-NTU) vs. calculated raw 3BDA index value (WV2Be162Bsub) with Pearson's r^2 ($r^2 = 0.699$, $p < 0.001$, $N = 29$ to avoid shorelines) (7b). Evaluation via observed (Y axis = Turbidity-NTU) vs. calculated turbidity concentration (WV2Be162Bsubturb) with Pearson's r^2 ($r^2 = 0.699$, $p < 0.001$, $N = 29$ to avoid shorelines) (7c). Details of the synthetic bands and band math are available in Tables 1, 2 and SI1 respectively.

commonly available at the 250 m spatial resolution and are part of the better performing algorithm (MODISTurbMoore80Red). The large pixel sizes associated with MODIS limit its use to relatively large water bodies and require severe masking to avoid mixed pixels.

None of the spectrally-oriented semi-analytical (spectral signature based) algorithms considered here had acceptable performance (Pearson's $r^2 > 0.600$) with regard to turbidity estimation with this sensor in this experiment due to the wide MODIS bands. While MODIS

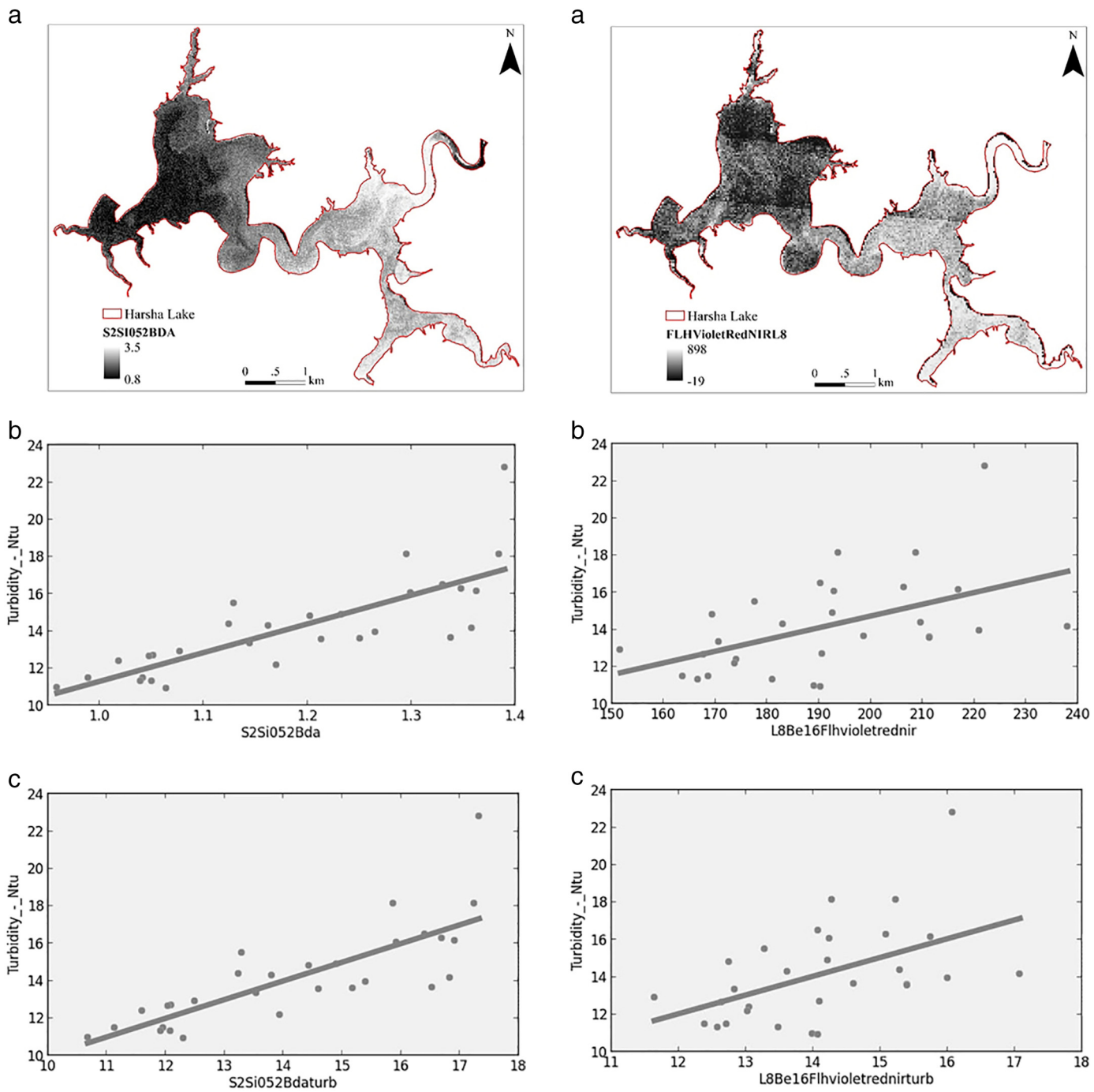


Fig. 8. Results of S2Si052BDA algorithm converted to turbidity values as applied to synthetic Sentinel-2 imagery with brighter pixels in the reservoir indicating higher turbidity (8a). Evaluation via observed (Y axis = Turbidity-NTU) vs. calculated raw index value (S2Si052BDA) with Pearson's r^2 ($r^2 = 0.624$, $p < 0.001$, $N = 29$ to avoid shorelines) (8b). Evaluation via observed (Y axis = Turbidity-NTU) vs. calculated turbidity concentration (S2Si052BDAPHY) with Pearson's r^2 ($r^2 = 0.624$, $p < 0.001$, $N = 29$ to avoid shorelines) (8c). The CASI data allowed the synthesis of Sentinel-2 bands 2 through 9 only. Details of the synthetic bands and band math are available in Tables 1, 2 and SI1 respectively.

could be a part of operational monitoring systems for cyanobacterial blooms and turbidity in general, its wide bands and coarse spatial resolution suggest that it will have limited value in operational monitoring systems for inland water quality, especially for smaller water bodies less than a few kilometers across. Index imagery with raw and normalized index Type 1 (Pearson's r) linear regressions are shown for the best performing algorithm (MODISTurbMoore80Red) in Fig. 10.

Fig. 9. Results of new L8Be16FLHVioletRedNIR algorithm as raw index values as applied to synthetic Landsat 8 imagery with brighter pixels in the reservoir indicating higher turbidity (9a). Evaluation via observed (Y axis = Turbidity-NTU) vs. calculated raw index value (L8Be16FLHVioletRedNIR) with Pearson's r^2 ($r^2 = 0.256$, $p = 1.004$, $N = 29$ to avoid shorelines) (9b). Evaluation via observed (Y axis = turbidity-NTU) vs. calculated turbidity concentration (L8Be16FLHVioletRedNIRPHY) with Pearson's r^2 ($r^2 = 0.256$, $p = 1.004$, $N = 29$ to avoid shorelines) (9c).

MERIS (synthetic)

We applied 30 existing and 3 new algorithms for turbidity estimation to synthetic MERIS/OLCI data for Harsha Lake with limited success (Tables 2 and ESM S1, Fig. 11) before severe masking. Sixteen of the turbidity, phycocyanin and Chl-a spectrally-oriented semi-analytical algorithms considered here had acceptable performance (Pearson's $r^2 > 0.600$) with regard to turbidity estimation with this sensor in this experiment after severe masking. In order of decreasing performance, the

MERISTurbDox02NIRoverRed, MERISBe16NDPhyI, MERISM12NDCI, MERISWY08CI, MERISM092BDA, MERISSI052BDA, MERISBe162B709sub601 and MERISHu103BDA, MERISBe16FLHblue, MERISBe16FLHBlueRedNIR, MERISTurbMoore80Red, MERISHarr92NIR, MERISSY002BDA, MERISAL10SABI, MERISTurbChip09NIRoverGreen and MERISBe16FLHPhy turbidity algorithms all estimated turbidity well in this experiment. We agree that MERIS/OLCI can be a part of

operational water quality monitoring systems (Wynne et al., 2012). However, high-spatial resolution CASI data shows that there was significant spatial heterogeneity in the concentration of turbidity on a scale much finer than either MERIS (300 m) or MODIS (250 m) pixels (Fig. 6a). Index imagery with raw and normalized index Type 1 (Pearson's r) linear regressions are shown for the best performing algorithm (MERISTurbDox02NIRoverRed) in Fig. 11. The regressions used only those pixels completely within the outline of Harsha Lake to avoid mixed land/water pixels.

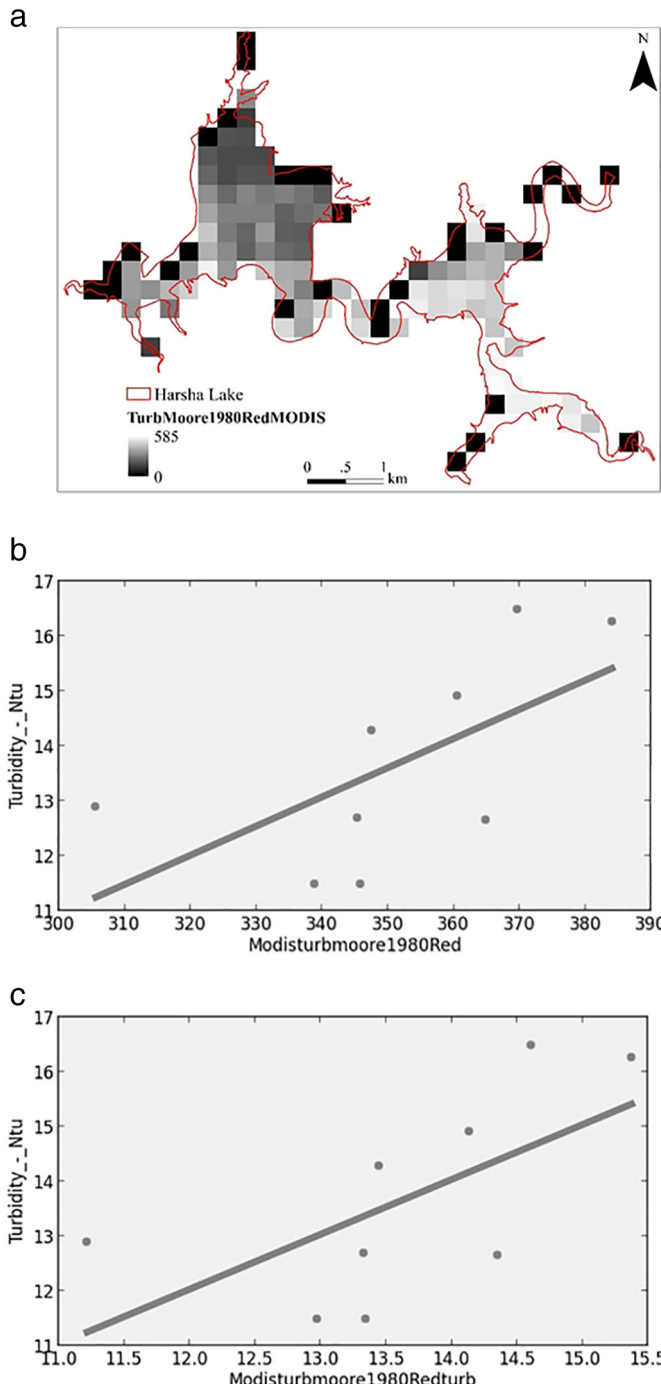


Fig. 10. Results of MODISTurbMoore80Red algorithm (Moore, 1980) converted to turbidity values as applied to synthetic MODIS imagery with brighter pixels in the reservoir indicating higher turbidity (10a). Evaluation as raw index values as applied to synthetic MODIS imagery and its evaluation via observed (Y axis = Turbidity-NTU) vs. calculated raw index value (MODISTurbMoore80Red) with Pearson's r^2 ($r^2 = 0.394, p = 1.002, N = 9$ due to large pixels) (10b). Evaluation via observed (Y axis = Turbidity-NTU) vs. calculated turbidity concentration (MODISTurbMoore80RedPHY) with Pearson's r^2 ($r^2 = 0.394, p = 1.002, N = 9$ due to large pixels) (10c).

Imager/algorith combination performance comparison

Examples of the best performing algorithms listed above in map form and as graphs of raw index values, normalized index values, zoomed and at the same scales are presented side by side in ESM Fig. S1. Traditional Type 1 Pearson's r^2 linear regression values as well as additional Type 1 Standard Error of Regression (Standard Error of Estimate or S values) and associated statistics (Table 3) as well as the Type 2 geometric mean regressions (Peltzer, 2015) (Table 4) for each of the imager/algorith combinations described above show an ordering of correlation identical to those of Pearson's r Type 1 regressions (Kudela et al., 2015a, b; Pinerio et al., 2008).

Finally, as a fourth type of statistical test of our results, we ran a repeat k-folds cross validation (Picard and Cook, 1984; Stone, 1974) for turbidity estimates from the real CASI aircraft data and for the WorldView-2, Sentinel-2 and Landsat-8 synthetic satellite data ($n = 29$) against in situ measurement/sample values (NTU) to avoid using the same data set for both calibration and validation. This is despite the fact that this study uses synthetic satellite imagery for algorithm comparison, not calibration and validation of real satellite imagery. The paired imager/algorith estimate and in situ measurement/sample pairs for the synthetic MERIS and MODIS imager were too few ($n = 9$) for the k-folds analysis. We limited our k-folds analysis to the real CASI aircraft and WorldView-2, Sentinel-2, and Landsat-8 synthetic imagery ($n = 29$) accordingly. The k-folds cross validation separated our pairs of in situ turbidity measurements (NTU) and normalized turbidity estimates from real CASI and synthetic satellite imagery into thirds as is standard practice (Picard and Cook, 1984; Stone, 1974). The method then uses two groups (two thirds of the paired values) as calibration and the third as validation. This is done for all combinations (3 models), then repeated using new groups randomly assigned over 5 iterations. The final result is average r^2 , Root Mean Squared Error (RMSE), and mean absolute error (MAE) values for each normalized imager/algorith index estimate vs. in situ turbidity measurement (NTU).

The resulting performance rankings of the k-fold cross validation test are also remarkably similar to those of the other three sets of statistical analyses (Pearson's r, geometric and Standard Error of Estimate tests) for real CASI data to in situ turbidity measurements (ESM Table S5). Differences in r^2 ranking within and between each method are usually within the second and sometimes third decimal places. All four types of statistical methods (Pearson's r, Standard Error of Regression (Standard Error of Estimate or S), Geometric Mean Tests, and k-fold cross validation tests) used here to compare in situ turbidity (NTU) values with normalized imager/algorith index estimates result in imager/algorith performance rankings that are remarkably similar and suggest that simple Pearson's r^2 and p values will be adequate for operational purposes if researchers and water quality managers collect enough in situ water quality measurements or water samples for laboratory analysis ($n = 29$ or more) for sub 30 m GSD imagery from water bodies or parts of water bodies that are approximately the size of Harsha Lake and if those in situ measurements and laboratory samples are collected coincident with image acquisition. This appears to be the case for Chl-a (Johansen et al., 2018). Evaluation of the portability of the imager/algorith combinations for turbidity estimation are underway.

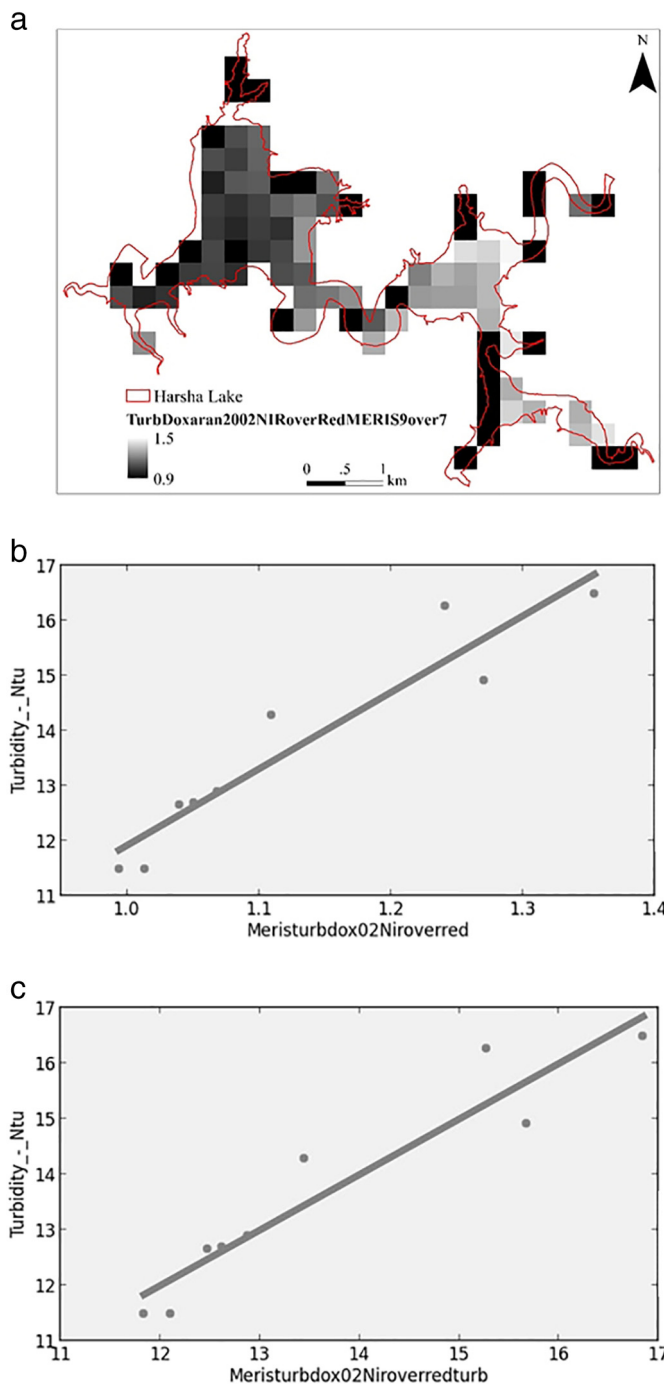


Fig. 11. Results of MERISTurbDox02NIRoverRed algorithm as raw turbidity index values as applied to synthetic MERIS imagery with brighter pixels in the reservoir indicating higher turbidity (11a). Evaluation via observed (Y axis = Turbidity-NTU) vs. raw turbidity index values (MERISTurbDox02NIRoverRed) concentration with Pearson's r^2 ($r^2 = 0.897$, $p < 0.001$, $N = 9$ due to large pixels) (11b). Evaluation via observed (Y axis = Turbidity-NTU) vs. calculated turbidity (MERISTurbDox02NIRoverRed) concentration with Pearson's r^2 ($r^2 = 0.897$, $p < 0.001$, $N = 9$ due to large pixels) (11c). Details of the synthetic bands and band math are available in Tables 1, 2 and SI1 respectively.

Discussion

The preceding results for real CASI hyperspectral aircraft data and isochronous synthetic multispectral satellite data compared to dense in situ measurements/samples are summarized in ESM Tables S2, S3, SI4 and SI6 and show that both direct (designed for purpose) and indirect (proxy) semi-analytical algorithms worked well with regard to turbidity estimation for Harsha Lake at the time of this experiment. As will

be shown below, this experiment also showed strong co-variance of turbidity-NTU values with BGA-PC-Cells/mL and total suspended solids and Chl-a values. These findings help to explain why several of the algorithms listed above in Tables 2 and ESM S1 had good performance with regard to turbidity as well as BGA and Chl-a estimation in Harsha Lake at the time of this experiment.

Direct vs. indirect turbidity indices

The focus of this study is on simple, portable, semi-analytical algorithms based on the red sediment turbidity, BGA/PC, and Chl-a spectral signatures for the estimation of general turbidity in the context of potentially harmful algal blooms including cyanobacteria. Algorithms specifically tuned to the red sediment turbidity feature had the best (but limited) performance only for Landsat-8 (L8Be16FLHVioletRedNIR), MODIS (MODISTurbMoore80Red) and MERIS (MERISTurbDox02NIRoverRed) as shown in Tables 3, 4 and ESM S4. Indirect turbidity index algorithms designed to measure phycocyanin had the best performance with CASI (CASIBe16NDPhyl), WorldView-2 (WV2Be162Bsub) and Sentinel-2 (S2SI052BDA) with regard to turbidity estimation and with regard to BGA estimation in this experiment as shown in Tables 3, 4 and ESM S4 suggesting that most of the turbidity was caused by cyanobacteria. The strong performance of semi-analytical, phycocyanin- and Chl-a- spectrum-based algorithms with regard to turbidity estimation is certainly due to the strong covariance of BGA and Chl-a with turbidity at the time of the experiment. In other words, the best algorithm for turbidity estimation depends upon the relative concentrations of spectrally-active pollutants in the water column at the time of image acquisition (Doxaran et al., 2002). In this case turbidity is also a reasonable proxy for BGA and Chl-a values as shown in Tables 5 and 6 below.

Co-varying water quality parameters

This study measured 41 water quality parameters (ESM Table S6) at each of the 44 surface observation sites during the hyperspectral overpass. We used this information to determine when and why some proxy algorithms such as those for phycocyanin and Chl-a also worked for turbidity estimation. Two sites were omitted from the Chl-a statistics during EPA quality control based on extremely low phaeophytin absorbance and Chl-a absorbance values after filtering and extraction in the laboratory. Our results show that several other water quality parameters were also correlated with turbidity-NTU values in Harsha reservoir at the time of hyperspectral image acquisition (Table S7). Eleven water quality parameters had Pearson's r^2 values >0.500 . They were, in order of decreasing correlation, BGA-PC-Cells/mL ($r^2 = 0.865$), BGA-PC-RFU ($r^2 = 0.864$), total suspended solids (TSS) ($r^2 = 0.711$), Rpe_a_µg/L ($r^2 = 0.645$), SumReChLµg/L ($r^2 = 0.600$), RCHLc_µg/L ($r^2 = 0.582$), DRP_µgPL ($r^2 = 0.562$), TDP_µg/L ($r^2 = 0.545$), SumRCHLµg/L ($r^2 = 0.543$), HCO3_ppm ($r^2 = 0.526$) and VSS_mgL ($r^2 = 0.524$) (Tables 5 and 6). Of these parameters, only BGA-PC-Cells, BGA-PC-RFU, TSS, Rpe_a_µg/L, SumReChLµg/L, RCHLc_µg/L, and SumRCHLµg/L and VSS are spectrally active. Nonetheless, their strong correlation with spectrally inactive water constituents explains why local empirical regressions against band reflectance values can be used to locally estimate a number of water quality parameters after local calibration (Ogashawara et al., 2013; Wheeler et al., 2012; Trescott, 2012; Wozniak et al., 2016).

In this particular lake, at this particular time, the high in situ BGA concentrations, are directly related to the abundance of cyanobacteria, made turbidity, BGA and Chl-a rough mutual proxies. Microscopic analyses of phytoplankton samples collected during this survey confirm the dominance of cyanobacteria during this particular experiment (ESM Table S8).

In summary there were several semi-analytical (spectrally-based) imager/algorithm combinations capable of estimating turbidity (and

Table 5

Water Quality Parameters Investigated for correlation with turbidity.

Constituent (unit)	Description	Method	Reference
Alkalinity mg as CaCO ₃	as is	Standard Methods 2320B	APHA 1999. 2320B Alkalinity. Standard Methods for the Examination of Water and Wastewater. American Public Health Association, American Water Works Association, Water Environment Federation.
BGA-PC - Cells/mL	Phycocyanin probe response as cell density in vivo fluorescence	YSI 2012. 6131 Blue-green Algae-Phycocyanin Probe	YSI 2012. 6-series Multiparameter Water Quality Sondes: User Manual. Environmental Monitoring Systems Operations Manual. YSI Incorporated, Yellow Springs, OH.
BGA-PC - RFU	Phycocyanin probe response as relative fluorescence unit	YSI 2012. 6131 Blue-green Algae-Phycocyanin Probe	YSI 2012. 6-series Multiparameter Water Quality Sondes: User Manual. Environmental Monitoring Systems Operations Manual. YSI Incorporated, Yellow Springs, OH.
Chl- μ g/L	Chlorophyll probe response as concentration	YSI 2012. 6025 Chlorophyll Probe	YSI 2012. 6-series Multiparameter Water Quality Sondes: User Manual. Environmental Monitoring Systems Operations Manual. YSI Incorporated, Yellow Springs, OH.
Chl-RFU	Chlorophyll probe response as relative fluorescence unit	YSI 2012. 6025 Chlorophyll Probe	YSI 2012. 6-series Multiparameter Water Quality Sondes: User Manual. Environmental Monitoring Systems Operations Manual. YSI Incorporated, Yellow Springs, OH.
Depth - m	as is	YSI 2012. 6600 V2-2 Vented Depth Sensor	YSI 2012. 6-series Multiparameter Water Quality Sondes: User Manual. Environmental Monitoring Systems Operations Manual. YSI Incorporated, Yellow Springs, OH.
DNH4 (μ gN/L)	Dissolved Ammonium	Ammonia phenolate method after filtering in the field	Smith P. 2001. Determination of ammonia (phenolate) by flow injection analysis colorimetry: Quikchem method 10-107-06-1-B. Lachat Instruments, Loveland, CO.
DNO2-3 (μ gN/L)	Dissolved Nitrite-Nitrate	Nitrate-nitrite, cadmium reduction after filtering in the field	Wendt K. 1995. Determination of nitrate/nitrite in surface and wastewaters by flow injection analysis: Quickchem Method 10-107-04-1-A. Lachat Instruments, Loveland, CO.
DOC (mg/L)	Dissolved organic Carbon	Wet oxidation after filtering in the field	EPA methods 415.1 and 9060 by wet oxidation UV/persulfate using a Phoenix 8000 (Tekmar-Dohrmann)
DRP (μ gP/L)	Dissolved Reactive Phosphorous (or filtered Ortho-P)	Molybdate method after filtering in the field	Sardina A. 2000. Determination of orthophosphate by flow injection analysis colorimetry: Quickchem Method 10-115-01-1-B. Lachat Instruments, Loveland, CO.
hardness mg as CaCO ₃	as is	Standard Methods 2340C	APHA 1999. 2340C Hardness. Standard Methods for the Examination of Water and Wastewater. American Public Health Association, American Water Works Association, Water Environment Federation.
HCO3- (est) (ppm)	Bicarbonate ion concentration (mg/l)	By calculation using pH and Alkalinity	APHA 1999. 2320B Alkalinity. Standard Methods for the Examination of Water and Wastewater. American Public Health Association, American Water Works Association, Water Environment Federation.
Microcystin-LR equivalent	Microcystin LR equivalents measured by ELISA as concentration (PPB)	ELISA method	USEPA 2016. Method 546: Determination of Total Microcystins and Nodularins in Drinking Water and Ambient Water by Adda Enzyme-Linked Immunosorbent Assay. EPA 815-B-16-011. Office of Ground Water and Drinking Water, Cincinnati, OH.
ODO - mg/L	Optical Dissolved Oxygen probe measurement as concentration	YSI 2012. 6150 Optical Dissolved Oxygen Probe	YSI 2012. 6-series Multiparameter Water Quality Sondes: User Manual. Environmental Monitoring Systems Operations Manual. YSI Incorporated, Yellow Springs, OH.
ODO Sat %	Optical Dissolved Oxygen probe measurement as percent saturation	YSI 2012. 6150 Optical Dissolved Oxygen Probe	YSI 2012. 6-series Multiparameter Water Quality Sondes: User Manual. Environmental Monitoring Systems Operations Manual. YSI Incorporated, Yellow Springs, OH.
OM percent (% OM)	% organic matter of suspended solids	calculated after loss on ignition gravimetric analysis	USEPA 2001. Method 1684. Total, Fixed and Volatile Solids in Water, Solids, and Biosolids. EPA-821-R-01-015. Washington, DC.
pH	as is	YSI 2012. 6561 pH Probe	YSI 2012. 6-series Multiparameter Water Quality Sondes: User Manual. Environmental Monitoring Systems Operations Manual. YSI Incorporated, Yellow Springs, OH.
PN (μ gN/L)	Particulate Nitrogen	Difference between TN and TDN	Patton, C.J. and J.R. Kryskalla. 2003. Methods of Analysis by the U.S. Geological Survey National Water Quality Laboratory - Evaluation of Alkaline Persulfate Digestion as an Alternative to Kjeldahl Digestion for Determination of Total and Dissolved Nitrogen and Phosphorus in Water. Water Resources Investigations Report 03-4174, USGS, Denver, CO.
POC (mg/L)	Particulate Organic Carbon	Difference between TOC and DOC	EPA methods 415.1 and 9060 by wet oxidation UV/persulfate using a Phoenix 8000 (Tekmar-Dohrmann)
PP (μ gP/L)	Particulate Phosphorous	Difference between TP and TDP	Prokopy WR. 1992. Determination of total phosphorus by flow injection analysis colorimetry (acid persulfate digestion method): QuikChem® Method 10-115-01-1-F. Lachat Instruments, 5600 Lindburgh Drive, Loveland, Colorado 80,539.
PRP (μ gP/L)	Particulate Reactive Phosphorous	Difference between TRP and DRP	Prokopy WR. 1992. Determination of total phosphorus by flow injection analysis colorimetry (acid persulfate digestion method): QuikChem® Method 10-115-01-1-F. Lachat Instruments, 5600 Lindburgh Drive, Loveland, Colorado 80,539.
RCe,a (μ g/L)	Phaeophytin Corrected Chlorophyll A measured as absorbance on filtered and extracted samples	Spectrophotometry after acetone extraction of filters	APHA 1999.10200H. Chlorophyll. Standard Methods for the Examination of Water and Wastewater. American Public Health Association, American Water Works Association, Water Environment Federation.
RCHLa (μ g/L)	Uncorrected Chlorophyll A measured as absorbance on filtered and extracted samples	Spectrophotometry after acetone extraction of filters	Jeffrey, S.W. & G.F. Humphrey. 1975. New spectrophotometric equations for determining chlorophylls a, b, and c, in higher plants, algae and natural phytoplankton. Biochem. Physiol. Pflanzen 167: 191. In: APHA 1999.10200H. Chlorophyll. Standard Methods for the Examination of

(continued on next page)

Table 5 (continued)

Constituent (unit)	Description	Method	Reference
RCHLb (µg/L)	Uncorrected Chlorophyll B measured as absorbance on filtered and extracted samples	Spectrophotometry after acetone extraction of filters	Water and Wastewater. American Public Health Association, American Water Works Association, Water Environment Federation. Jeffrey, S.W. & G.F. Humphrey. 1975. New spectrophotometric equations for determining chlorophylls a, b, and c, in higher plants, algae and natural phytoplankton. <i>Biochem. Physiol. Pflanzen</i> 167: 191. In: APHA 1999.10200H. Chlorophyll. Standard Methods for the Examination of Water and Wastewater. American Public Health Association, American Water Works Association, Water Environment Federation.
RCHLc (µg/L)	Uncorrected Chlorophyll C measured as absorbance on filtered and extracted samples	Spectrophotometry after acetone extraction of filters	Jeffrey, S.W. & G.F. Humphrey. 1975. New spectrophotometric equations for determining chlorophylls a, b, and c, in higher plants, algae and natural phytoplankton. <i>Biochem. Physiol. Pflanzen</i> 167: 191. In: APHA 1999.10200H. Chlorophyll. Standard Methods for the Examination of Water and Wastewater. American Public Health Association, American Water Works Association, Water Environment Federation.
SUM RCHL (µg/L)	Sum Extracted CHL - using Standard Method and Trichromatic Equation (zeroing negative values for CHL-B before summing)	Spectrophotometry after acetone extraction of filters	Jeffrey, S.W. & G.F. Humphrey. 1975. New spectrophotometric equations for determining chlorophylls a, b, and c, in higher plants, algae and natural phytoplankton. <i>Biochem. Physiol. Pflanzen</i> 167: 191. In: APHA 1999.10200H. Chlorophyll. Standard Methods for the Examination of Water and Wastewater. American Public Health Association, American Water Works Association, Water Environment Federation.
RCe,a (µg/L)	Phaeophytin Corrected Chlorophyll A measured as absorbance on filtered and extracted samples	Spectrophotometry after acetone extraction of filters	Lorenzen, C.J. 1967. Determination of chlorophyll and pheo-pigments: spectrophotometric equations. <i>Limnol. Oceanogr.</i> 12:343. In: APHA 1999.10200H. Chlorophyll. Standard Methods for the Examination of Water and Wastewater. American Public Health Association, American Water Works Association, Water Environment Federation.
RPe,a (µg/L)	Phaeophytin measured as absorbance on filtered and extracted samples	Spectrophotometry after acetone extraction of filters	Lorenzen, C.J. 1967. Determination of chlorophyll and pheo-pigments: spectrophotometric equations. <i>Limnol. Oceanogr.</i> 12:343. In: APHA 1999.10200H. Chlorophyll. Standard Methods for the Examination of Water and Wastewater. American Public Health Association, American Water Works Association, Water Environment Federation.
SUM ReCHL (µg/L)	Sum of RCe,a and RPe,a	Spectrophotometry after acetone extraction of filters	Lorenzen, C.J. 1967. Determination of chlorophyll and pheo-pigments: spectrophotometric equations. <i>Limnol. Oceanogr.</i> 12:343. In: APHA 1999.10200H. Chlorophyll. Standard Methods for the Examination of Water and Wastewater. American Public Health Association, American Water Works Association, Water Environment Federation.
SpCond - µS/cm	Specific Conductance in microsiemens per cm	YSI 2012. 6560 Conductivity/Temperature Probe	YSI 2012. 6-series Multiparameter Water Quality Sondes: User Manual. Environmental Monitoring Systems Operations Manual. YSI Incorporated, Yellow Springs, OH.
TDN (µgNL)	Total Dissolved Nitrogen	Wet digestion with alkaline persulfate after filtering in the field	APHA. 2001. American Public Health Association-Standard Methods for the Examination of Water and Wastewater, 20th Edition. United Book Press, Baltimore, MD.
TDP (µgP/L)	Total Dissolved Phosphorous	Wet digestion with acid persulfate after filtering in the field	Prokopy WR. 1992. Determination of total phosphorus by flow injection analysis colorimetry (acid persulfate digestion method): QuikChem® Method 10-115-01-1-F. Lachat Instruments, 5600 Lindburgh Drive, Loveland, Colorado 80,539.
Temp - °C	as is	YSI 2012. 6560 Conductivity/Temperature Probe	YSI 2012. 6-series Multiparameter Water Quality Sondes: User Manual. Environmental Monitoring Systems Operations Manual. YSI Incorporated, Yellow Springs, OH.
TN (µgN/L)	Total Nitrogen	Wet digestion with alkaline persulfate on whole sample	Patton, C.J. and J.R. Kryskalla. 2003. Methods of Analysis by the U.S. Geological Survey National Water Quality Laboratory - Evaluation of Alkaline Persulfate Digestion as an Alternative to Kjeldahl Digestion for Determination of Total and Dissolved Nitrogen and Phosphorus in Water. Water Resources Investigations Report 03-4174, USGS, Denver, CO.
TNH4 (µgN/L)	Total Ammonium	Ammonia phenolate method on whole sample	Smith P. 2001. Determination of ammonia (phenolate) by flow injection analysis colorimetry: Quikchem method 10-107-06-1-B. Lachat Instruments, Loveland, CO.
TOC (mg/L)	Total Organic Carbon	Wet oxidation on whole sample	EPA methods 415.1 and 9060 by wet oxidation UV/persulfate using a Phoenix 8000 (Tekmar-Dohrmann)
TP (µgP/L)	Total Phosphorous	Wet digestion with acid persulfate on whole sample	Prokopy WR. 1992. Determination of total phosphorus by flow injection analysis colorimetry (acid persulfate digestion method): QuikChem® Method 10-115-01-1-F. Lachat Instruments, 5600 Lindburgh Drive, Loveland, Colorado 80,539.
TRP (µgP/L)	Total Reactive Phosphorous (or Unfiltered Ortho-P)	Molybdate method on whole sample	Sardina A. 2000. Determination of orthophosphate by flow injection analysis colorimetry: Quickchem Method 10-115-01-1-B. Lachat Instruments, Loveland, CO.
TSS (mg/L)	Total Suspended Solids	Gravimetric, Dried at 103–105 °C	Total Suspended Solids (TSS) EPA Method 160.2 (Gravimetric, Dried at 103–105 °C)
Turbidity - NTU	as is	YSI 2012. 6136 Turbidity Probe	YSI 2012. 6-series Multiparameter Water Quality Sondes: User Manual. Environmental Monitoring Systems Operations Manual. YSI Incorporated, Yellow Springs, OH.
VSS (mg/L)	Volatile Suspended Solids	solid material combustible at 550 °C	USEPA 2001. Method 1684. Total, Fixed and Volatile Solids in Water, Solids, and Biosolids. EPA-821-R-01-015. Washington, DC.

Table 6

Correlation of water quality parameters with turbidity-NTU as measured by Pearson's r test.

Algorithms	r^2	p value	Slope	Intercept
BGA_PC_Cells	0.8653074	5.19E-19	0.0002623	7.4502632
BGA_PC_RFU	0.863909	6.38E-19	0.6602333	7.6186241
TSS_mgL	0.7112863	2.38E-12	1.0536762	3.5509267
Rpe_a_µgL	0.6449183	1.56E-10	0.2311425	11.796019
SumReCHLµgL	0.6008639	1.68E-09	0.163247	6.0799108
RCHLc_µgL	0.5824032	4.20E-09	1.2471218	8.901876
DRP_µgPL	0.5622411	1.10E-08	0.3594458	10.412115
TDP_µgPL	0.5449048	2.42E-08	0.1977696	11.475227
SumRCHLµgL	0.542994	2.64E-08	0.1670745	5.5827007
HCO3_ppm	0.5260809	5.53E-08	0.4112644	-14.329758
VSS_mgL	0.5241072	6.02E-08	1.2921568	3.1978112
Chl_RFU	0.498049	1.79E-07	2.2197324	9.538611
Chl_µgL	0.4946306	2.06E-07	0.4208989	10.402754
RCHLc_µgL	0.4709735	5.25E-07	0.1812306	5.6787151
alkalinity_mg_CaCO3	0.4229773	3.13E-06	0.2522569	-6.3363179
TP_µgPL	0.4021038	6.52E-06	0.0621394	8.9804889
OM_percent	0.3580531	2.85E-05	-0.2906501	39.199187
RCHLb_µgL	0.2905384	2.31E-04	1.5740605	14.028412
SpCond_mS_cm	0.2506685	7.33E-04	0.1616225	-26.896014
PP_µgPL	0.2378878	1.05E-03	0.0643636	9.7393857
pH	0.1559075	9.66E-03	5.0948823	-36.509686
hardness_mg_CaCO3	0.1438857	1.32E-02	0.1326477	0.2849891
Temp	0.1388383	1.51E-02	-1.6416568	61.988324
TOC_mgL	0.1281197	1.99E-02	7.1466773	-38.06652
ODO_mgL	0.1212867	2.38E-02	0.4397092	7.0258823
Rce:a_µgL	0.1057996	3.56E-02	0.1188258	9.6893876
ODO_Sat_per	0.0954587	4.65E-02	0.0291277	8.0439998
DOC_mgL	0.0757423	7.77E-02	4.2555382	-14.543035
PN_µgNL	0.0738393	8.17E-02	0.0027752	12.679153
TN_µgNL	0.0728495	8.39E-02	0.002708	11.165929
TRP_µgPL	0.0558864	1.32E-01	0.0488274	13.111396
TNH4_µgNL	0.0494976	1.57E-01	-0.0415785	15.194841
Microcystin_LR	0.0468236	1.69E-01	0.641401	11.420034
DNO2.3_µgNL	0.0303256	2.70E-01	-0.0726013	14.918747
DNH4_µgNL	0.02751	3.00E-01	-0.0995275	15.373474
pH_Alkalinity	0.0123244	4.84E-01	3.1773116	-16.172059
PRP_µgPL	0.0090016	5.50E-01	-0.0204095	14.725157
TDN_µgNL	0.0005365	8.84E-01	0.0018247	13.361013
POC_mgL	8.169E-05	9.55E-01	-0.1767347	14.506014

BGA and Chl-a) in this small BGA-rich inland water body based on the real CASI and the synthetic WorldView-2/-3, Sentinel-2 and MERIS imagers and to a lesser extent with the Landsat-8 and MODIS imagers (this paper and Beck et al., 2016, 2017). At least in this experiment, the strong correlation of in situ turbidity and in situ BGA_PC_Cells ($r^2 = 0.865$, $p < 0.001$, $N = 42$) (Fig. 12) suggests that BGA was the primary source of turbidity at the time of the experiment and allows BGA and turbidity to be used as mutual proxies after field verification.

More modest co-variance of in situ turbidity and in situ TSS ($r^2 = 0.711$, $p < 0.001$, $N = 42$) (Fig. 13) suggests the near absence or masking of a red sediment reflectance peak (Doxaran et al., 2002) by chlorophyll-a, phycocyanin, and water absorption. This would explain the generally more modest performance of the red sediment ("Turb") algorithms in this particular experiment (Tables 2, ESM S1 and S4) relative to phycocyanin and Chl-a algorithms. Even more modest correlations of in situ turbidity with laboratory measurements of chlorophyll (Figs. 14 and 15) suggest that phycocyanin in blue green algae was more spectrally active than either chlorophyll or red sediment as might be expected during this near annual peak cyanobacterial bloom. This is consistent with a Manhattan distance analysis of Pearson's r^2 values followed by a Ward cluster analysis summarized as a heatmap (Fig. 16) (Raschka, 2016) of the 41 water quality parameters measured by the US EPA in this experiment shows BGA and Turbidity within a second level cluster with Chl, TSS, VSS and several forms of phosphorous in a third level cluster.

The one exception to this "cyanobacteria as turbidity generalization" was the good performance of the Moore red sediment algorithm with

MODIS which appears to benefit from a combination of a narrow band near the red sediment reflectance peak, large integrative pixels and a strong turbidity and BGA contrast between the eastern and western basins of Harsha reservoir at the time of the experiment. Studies with red sediment algorithms in less productive waters have yielded better performance (Barnes et al., 2015; Bowers and Binding, 2006; Chipman et al., 2009; Dogliotti et al., 2015; Doxaran et al., 2002; Guttler et al., 2013; Harrington et al., 1992; Lathrop et al., 1991; Moore, 1980; Nechad et al., 2010; Potes et al., 2012; Ruddick et al., 2008; Shen et al., 2012; Wu et al., 2014). The results of this experiment should be interpreted in the context of highly-productive, BGA-rich waters accordingly.

Once the most promising algorithms from this experiment have been tuned to the on-orbit radiometry of each real imager, we will be able to use Sentinel-2A and -2B and WorldView-2/-3 for operational turbidity estimation in these smaller productive waters. This situation should improve further as hyperspectral imagers such as HypsIRI are launched. The large pixel size of Sentinel-3/MERIS/OLCI will be most useful in water bodies larger than Harsha Lake.

Our Chl-a companion study (Beck et al., 2016) included an error budget for the radiometry of our real aircraft and synthetic satellite imagery that indicated radiometric uncertainties on the order of 200%. Similarly, our field (ASD) spectra could have radiometric uncertainties on the order of 800% based on previous sun glint and wave studies (Lee et al., 2010). Nonetheless, the very strong performance of several well-established turbidity, BGA and Chl-a algorithms with our atmospherically corrected hyperspectral aircraft imagery suggests that our methods were more than adequate for our "red flag" early warning purposes for local and regional water quality managers. For these reasons we expect the algorithm performance rankings to differ somewhat with real imagery. Therefore we have identified groups of promising imager/algorithm combinations accordingly (ESM Table S4) instead of relying on only one algorithm per imager or even a single imager/algorithm combination. We are confident of our overall results given the very strong performance of many well-established turbidity, BGA and Chl-a algorithms with our dense, coincident surface observations in this experiment.

Conclusions

This study used atmospherically corrected high-spatial and high-spectral resolution VNIR CASI hyperspectral imagery to construct synthetic WorldView-2, Sentinel-2, Landsat-8, MODIS and Sentinel-3 (MERIS/OLCI) image data sets with dense coincident surface observations in the form of in-situ water quality sonde and laboratory measurements made on grab water samples to evaluate the performance of reflectance algorithms for estimating turbidity in temperate productive

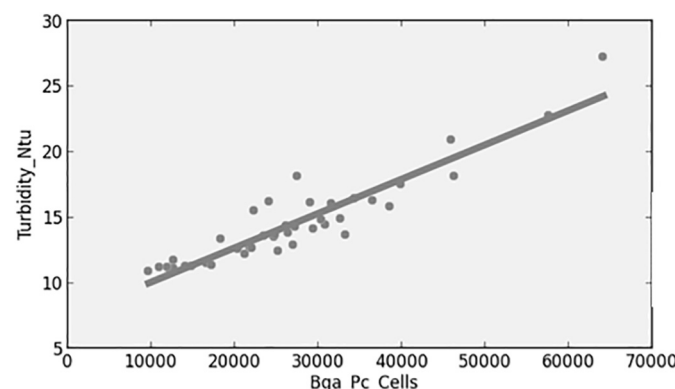


Fig. 12. Co-variance of turbidity (Turbidity-NTU) with BGA (BGA_PC_Cells/mL) as measured by in-water sondes with Pearson's r^2 ($r^2 = 0.865$, $p < 0.001$, $N = 42$). The strong contribution of BGA to turbidity at the time of image acquisition made turbidity and BGA mutual proxies in this experiment and may do so in other BGA-rich waters.

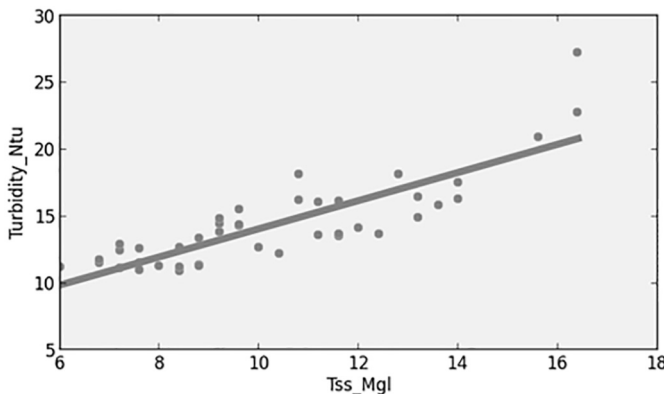


Fig. 13. Co-variance of turbidity (Turbidity-NTU) with Total Suspended Solids (TSS_mg/L) as measured by in-water sondes and laboratory analyses respectively with Pearson's r^2 ($r^2 = 0.711, p < 0.001, N = 42$). The secondary contribution of TSS to turbidity at the time of image acquisition explains why both red-sediment- and phycocyanin-based algorithms provided reasonable estimates of turbidity in this experiment and may do so in other BGA-rich waters.

inland (green turbid) waters. The study focused on currently operational and near-future imaging satellite constellations that may be suitable contributors to an operational water quality monitoring system for inland reservoirs, lakes and rivers.

We found that several established algorithms designed for the estimation of phycocyanin, Chl-a and turbidity performed well with regard to turbidity estimation for most of the synthetic satellite data sets considered here. The CASI Be16NDPhyI, CASIBe162B700sub601, CASISi052BDA, CASIMM12NDCIalt, and CASIMM122BDA algorithms worked well with CASI imagery. The WV2Be162Bsub, WV2Si052BDA, WV2Be16NDPhyI, WV2Mi092BDA and WV2Am092Bsub algorithms worked well with WorldView-2 and 3, the S2Si052BDA, S2MM12NDCI and S2Be162Bsub algorithms with Sentinel-2, and the MERISTurbDox02NIRoverRed, MERISBe16NDPhy, MERISMM12NDCI, MERISWY08CI, MERISMM092BDA, MERISSi052BDA, MERISBe162B709sub601, MERISHu103BDA, MERISBe16FLHblue, MERISBe16FLHBlueRedNIR, MERISTurbMoore80Red, MERISHarr92NIR, MERISSY002BDA, MERISAL10SABI, MERISTurbChip09NIRoverGreen and MERISBe16FLHPhy algorithms with MERIS-like imagery. The MODISTurbMoore80Red algorithm had limited performance with MODIS imagery and a new L8Be16FLHVioletRedNIR algorithm had limited performance with simulated Landsat-8 imagery. Si052BDA, MM12NDCI, WVBe162Bsub and CASIBe16NDPhyI were the most

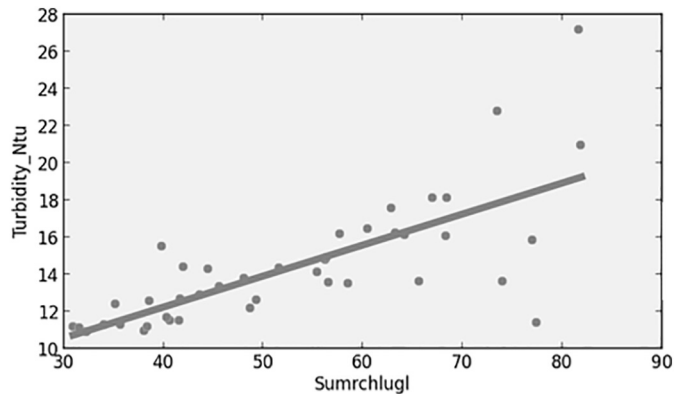


Fig. 15. Co-variance of turbidity (Turbidity-NTU) with SumRchl (SumRchl ($\mu\text{g/L}$)) chlorophyll as measured by in-water sondes and laboratory analyses respectively with Pearson's r^2 ($r^2 = 0.543, p < 0.001, N = 42$). The stronger correlations of turbidity with BGA and TSS listed above suggest that the phycocyanin and red sediment were more spectrally active than chlorophyll during this (near peak cyanobacterial bloom) experiment.

widely applicable (most portable) turbidity algorithms in this experiment.

Algorithm/imager combinations that include the phycocyanin reflectance minimum at 620 nm outperformed red sediment turbidity and Chl-a algorithms for turbidity estimation with CASI, WorldView-2 and Sentinel-2 and were only slightly less effective than red sediment ("Turb") algorithms for Landsat-8, MODIS and MERIS (Table S4). We used red sediment turbidity and Chl-a proxy algorithms to estimate turbidity with good results for MERIS/OLCI and limited results for Landsat-8 and MODIS for this water body at the time of hyperspectral image acquisition. Landsat-8 requires an alternative algorithm, such as the new turbidity "redness" L8Be16FLHVioletRedNIR algorithm. MERIS and MODIS do not capture the spatial heterogeneity in turbidity observed in this study due to their large pixels. MERIS/OLCI has a narrow red band centered at 665 nm that targets the red sediment/Chl-a absorption red region (Nechad et al., 2010) well and has good performance with regard to turbidity estimation with the simple MERISTurbDox02NIRoverRed algorithm accordingly. MODIS has wide bands that do not target the red sediment/Chl-a absorption red region as well and has lower performance accordingly (Tables 2, S1 and S3) although it may be useful with MODISTurbMoore80Red or MODISMM12NDCI for larger water bodies.

For imagers with appropriate band widths and positions relative to turbidity reflectance signatures simple algorithms that subtract or ratio bands, and, therefore, inherently normalize reflectance performed well and appear to be relatively portable between most existing and near-future satellite imaging systems for the estimation of turbidity (and BGA and Chl-a). Therefore, near-term steps toward operational water quality monitoring systems for inland water bodies smaller than a few kilometers across should focus on Sentinel-2 A and B, and to a lesser extent Landsat-8 with empirical tuning, with augmentation from WorldView-2 and -3 or hyperspectral imagery when required. MERIS/OLCI may also be useful for time-series monitoring but will capture very little of the spatial heterogeneity of turbidity in smaller inland water bodies. Future satellite imaging systems for cyanobacterial and turbidity monitoring in smaller inland water bodies that are often sources of drinking water should include narrow bands focused on the 620 nm phycocyanin absorption feature and the 665 nm red sediment/Chl-a reflectance/absorption feature (Doxaran et al., 2002; Mishra et al., 2009 2013; Moore, 1980; Nechad et al., 2010; Simis et al., 2005, 2007; Sun et al., 2015) and spatial resolutions of 20–90 m. Given the overlapping spectral signatures of red sediment, Chl-a and phycocyanin and variation in their relative contributions between water bodies, local calibration and validation will continue to be important. Indeed, in this experiment at Harsha Lake, BGA sonde values were

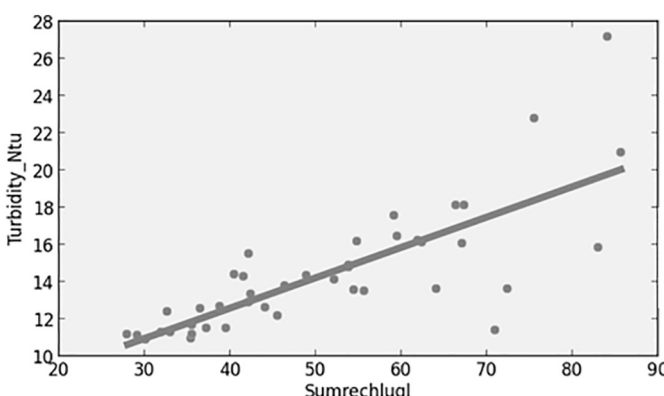


Fig. 14. Co-variance of turbidity (Turbidity-NTU) with SumRechl (SumRechl ($\mu\text{g/L}$)) chlorophyll as measured by in-water sondes and laboratory analyses respectively with Pearson's r^2 ($r^2 = 0.600, p < 0.001, N = 42$). The stronger correlations of turbidity with BGA and TSS listed above suggest that the phycocyanin and red sediment were more spectrally active than chlorophyll during this (near peak cyanobacterial bloom) experiment.

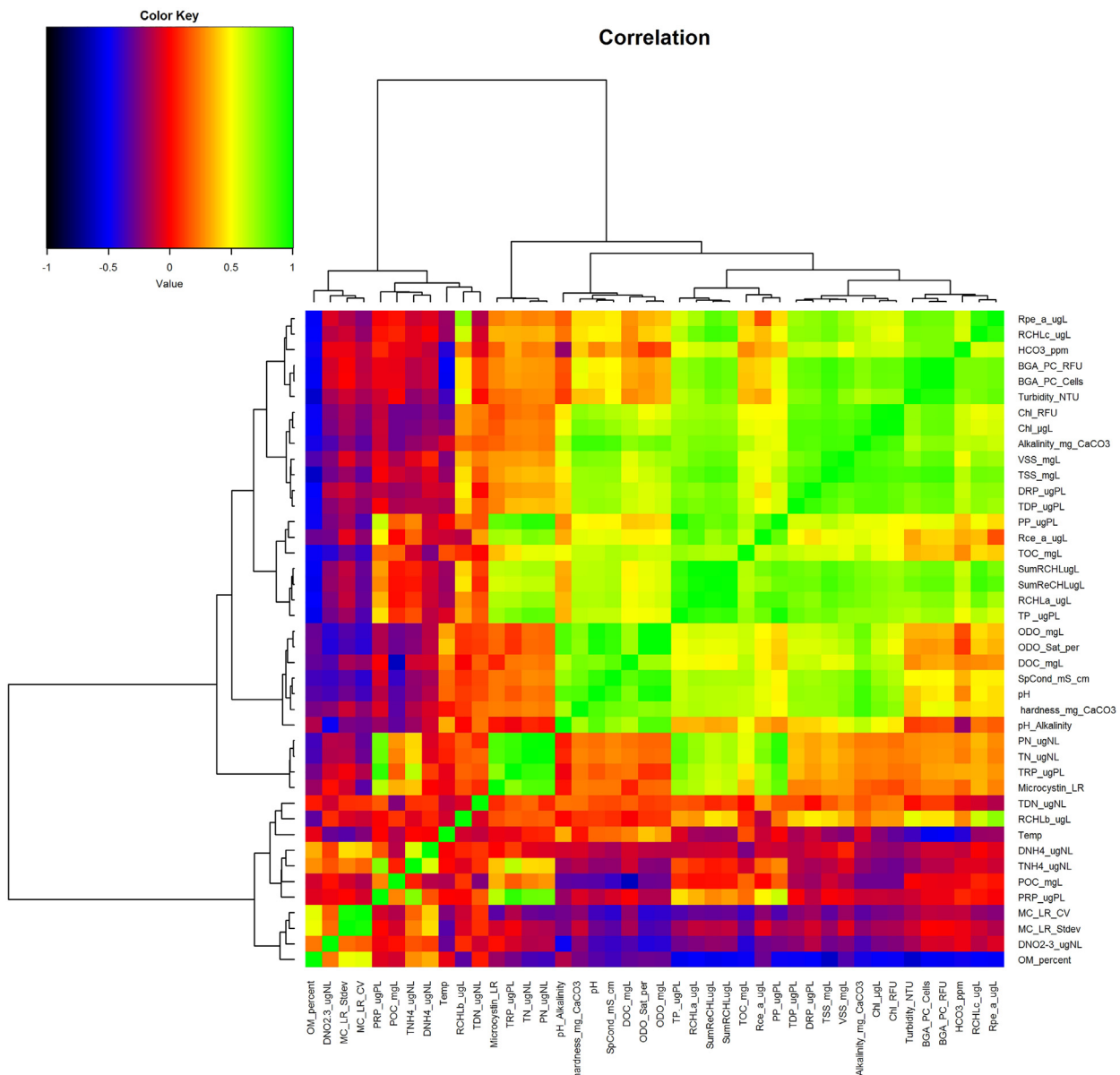


Fig. 16. Manhattan distance analysis of Pearson's R² values followed by a Ward cluster analysis summarized as a heatmap (Fig. 16) using code modified from [Raschka \(2016\)](#) of the 41 water quality parameters measured by the US EPA in this experiment. BGA and Turbidity are within a second level cluster with Chl, TSS, VSS and several forms of phosphorous in a third level cluster.

better turbidity proxies than TSS or laboratory or sonde measurements of Chl-a, b and c. Hence our advocacy of the generation of a number of standard products for local, state and regional interpretation by water quality managers.

Acknowledgments

This study was funded by the U.S. Army Corps of Engineers and the NASA Glenn Research Center. The U.S. Environmental Protection Agency and the Kentucky Department of Environmental Protection, Division of Water provided valuable in-kind services. Any use of trade, product, or firm names is for descriptive purposes only and does not imply endorsement by the U.S. Government. This article expresses only the personal views of the U.S. Army Corps of Engineers and U.S. EPA employees listed as authors and does not necessarily reflect the official positions of the Corps of the Department of the Army, or of the U.S. EPA, or NASA.

Appendix A. Supplementary data

Supplementary data to this article can be found online at <https://doi.org/10.1016/j.jglr.2018.09.001>.

References

- Alawadi, F., 2010. Detection of surface algal blooms using the newly developed algorithm surface algal bloom index (SABI). Proc. SPIE 7825. <https://doi.org/10.1117/12.862096>.

Amin, R., Zhou, J., Gilerson, A., Gross, B., Moshary, F., Ahmed, S., 2009. Novel optical techniques for detecting and classifying toxic dinoflagellate *Karenia brevis* blooms using satellite imagery. Opt. Express 17 (11), 1–13.

APHA, 2001. American Public Health Association—Standard Methods for the Examination of Water and Wastewater. 20th edition. United Book Press, Baltimore, MD.

Augusto-Silva, P.B., Ogashawara, I., Barbosa, C.C.F., de Carvalho, L.A.S., Jorge, D.S.F., Fornari, C.I., Stech, J.L., 2014. Analysis of MERIS reflectance algorithms for estimating chlorophyll-a concentration in a Brazilian reservoir. Remote Sens. 6, 11689–11707.

- Barnes, B.B., Hu, C., Kovach, C., Silverstein, R.N., 2015. Sediment plumes induced by the port of Miami dredging: analysis and interpretation using Landsat and MODIS data. *Remote Sens. Environ.* 170, 328–339.
- Beck, R.A., Frohn, R., South, R., Kriegel, K., Brunner, J., McLaughlin, J., Stanisz, M., Dobbins, J., Lambert, C., Miller, D., Ardire, P., Gray, D., Bridgeman, T., Lein, J., Capello, P., 2011. GeoTempo: a modular OGC sensor web. Association of Computing Machinery – IEEE – Proc. 2nd Int. Conf. on Computing for Geospatial Research & Applications Vol. 35, pp. 1–6.
- Beck, R.A., Zhan, S., Liu, H., Tong, S., Yang, B., Xu, M., Ye, Z., Huang, Y., Wu, Q., Wang, S., Berling, K., Murray, A., Emery, E., Reif, M., Harwood, J., Young, J., Nietch, C., Macke, D., Martin, M., Stillings, G., Stumpf, R., 2016. Comparison of satellite reflectance algorithms for estimating chlorophyll-a in a temperate reservoir using coincident hyperspectral aircraft imagery and dense coincident surface observations. *Remote Sens. Environ.* 178, 15–30.
- Beck, R.A., Zhan, S., Liu, H., Tong, S., Yang, B., Xu, M., Ye, Z., Huang, Y., Wu, Q., Wang, S., Berling, K., Murray, A., Emery, E., Reif, M., Harwood, J., Young, J., Nietch, C., Macke, D., Martin, M., Stillings, G., Stumpf, R., 2017. Comparison of satellite reflectance algorithms for estimating phycocyanin in a temperate reservoir using coincident hyperspectral aircraft imagery and dense coincident surface observations. *Remote Sens.* 9, 1–30.
- Binding, C.E., Greenberg, T.A., Bukata, R.P., 2013. The MERIS maximum chlorophyll index, its merits and limitations for inland water algal bloom monitoring. *J. Great Lakes Res.* 39, 100–107.
- Bowers, D.G., Binding, C.E., 2006. The optical properties of mineral suspended particles: a review and synthesis. *Estuar. Coast. Shelf S.* 67, 219–230. <https://doi.org/10.1016/j.ecss.2005.11.010>, 2006.
- Brezonik, P., Menken, K.D., Bauer, M., 2005. Landsat-based remote sensing of lake water quality characteristics, including chlorophyll and colored dissolved organic matter (CDOM). *Lake Reservoir Manag.* 21, 373–382.
- Cairns, S.H., Dickson, K.L., Atkinson, S.F., 1997. An examination of measuring selected water quality trophic indicators with SPOT satellite HRV data. *Photogr. Eng. Remote Sens.* 63, 263–265.
- Chipman, J.W., Olmanson, L.G., Gitelson, A.A., 2009. Remote Sensing Methods for Lake Management: A Guide for Resource Managers and Decision-Makers (Developed by the North American Lake Management Society in collaboration with Dartmouth College, University of Minnesota, and University of Nebraska for the United States Environmental Protection Agency).
- Dekker, A., 1993. Detection of the Optical Water Quality Parameters for Eutrophic Waters by High Resolution Remote Sensing. Free University, Amsterdam (Ph.D. Thesis).
- DigitalGlobe, 2009. WorldView-2 Data Sheet. pp. 1–2.
- DigitalGlobe, 2014. WorldView-3 Data Sheet. pp. 1–2.
- Dogliotti, A.I., Ruddick, K.G., Nechad, B., Doxaran, D., Knaeps, E., 2015. A single algorithm to retrieve turbidity from remotely-sensed data in all coastal and estuarine waters. *Remote Sens. Environ.* 156, 157–168.
- Doxaran, D., Froidefond, J.-M., Castaing, P., 2002. A reflectance band ratio used to estimate suspended matter concentrations in sediment-dominated coastal waters. *Int. J. Remote Sens.* 23, 5079–5085.
- Doxaran, D., Cherukuru, N., Lavender, S.J., 2006. Apparent and inherent optical properties of turbid estuarine waters: measurements, empirical quantification relationships, and modeling. *Appl. Opt.* 45 (10), 2310–2324.
- Duan, H., Ma, R., Hu, C., 2012. Evaluation of remote sensing algorithms for cyanobacterial pigment retrievals during spring bloom formation in several lakes of East China. *Remote Sens. Environ.* 126, 126–135.
- European Space Agency, 2012. MERIS Frequently Asked Questions. pp. 1–20.
- European Space Agency, 2013. Sentinel-2 Data Sheet. pp. 1–2.
- Feng, L., Hu, C., Han, X., Chen, X., Qi, L., 2015. Long-term distribution patterns of chlorophyll-a concentration in China's largest freshwater lake: MERIS full-resolution observations with a practical approach. *Remote Sens.* 7 (1), 275–299. <https://doi.org/10.3390/rs7010027>.
- Fraser, R.N., 1998. Hyperspectral remote sensing of turbidity and chlorophyll a among Nebraska Sand Hills lakes. *Int. J. Remote Sens.* 19, 1579–1589.
- Frohn, R.C., Autrey, B.C., 2007. Ohio River WAtter Quality Assessment Using Landsat-7 Data. ROHN, Presented at Surface Water Information Management System Conference, Chicago, IL, January 30 – February 01.
- Fuller, L.M., Aichele, S.S., Minnerick, R.J., 2004. Predicting water quality by relating secchi-disk transparency and chlorophyll *a* measurements to satellite imagery for Michigan inland lakes, August 2002. U.S. Geological Survey, Scientific Investigations Report 2004-5086, p. 25.
- Giardino, C., Brando, V.E., Dekker, A.G., Strömbeck, N., Candiani, G., 2007. Assessment of water quality in Lake Garda (Italy) using Hyperion. *Remote Sens. Environ.* 109, 183–195.
- Gitelson, A.A., Garbuзов, G., Szilagyi, F., Mittenzwey, K.H., Karniel, A., Kaiser, A., 1993. Quantitative remote sensing methods for real-time monitoring of inland waters quality. *Int. J. Remote Sens.* 14, 1269–1295.
- Gitelson, A.A., Gritz, U., Merzlyak, M.N., 2003. Relationships between leaf chlorophyll content and spectral reflectance and algorithms for non-destructive chlorophyll assessment in higher plant leaves. *J. Plant Phys.* 160, 271–282.
- Glasgow, H.B., Burkholder, J.M., Reed, R.E., Lewitus, A.J., Kleinman, J.E., 2004. Real-time remote monitoring of water quality: a review of current applications, and advancements in sensor technology, telemetry, and computing technologies. *J. Exp. Marine Biol. Ecol.* 300, 409–448.
- Gower, J.F.R., Brown, L., Borstad, G.A., 2004. Observation of chlorophyll fluorescence in west coast waters of Canada using the MODIS satellite sensor. *Can. J. Remote. Sens.* 30 (1), 17–25.
- Gower, J., King, S., Goncalves, P., 2008. Global monitoring of plankton blooms using MERIS MCI. *Int. J. Remote Sens.* 29, 6209–6216.
- Graham, J.L., 2006. Harmful algal blooms. USGS Fact Sheet, 2006–3147.
- Guttler, F.N., Niculescu, S., Gohin, F., 2013. Turbidity retrieval and monitoring of Danube Delta waters using multisensor optical remote sensing data: an integrated view from the delta plain lakes to the western-northwestern Black Sea coastal zone. *Remote Sens. Environ.* 132, 86–101.
- Han, L., Jordan, K., 2005. Measuring algal chlorophyll concentration in Pensacola Bay, Florida using Landsat ETM+ data. *Int. J. Remote Sens.* 26 (23), 5245–5254.
- Harrington Jr, J.A., Schiebe, F.R., Nix, J.F., 1992. Remote sensing of Lake Chicot, Arkansas: monitoring suspended sediments, turbidity, and Secchi depth with Landsat MSS data. *Remote Sens. Environ.* 39, 15–27.
- Heisler, J., Clibert, P., Burkholder, J., Anderson, D., Cochlan, W., Dennison, W., Dortch, Q., Gobler, C., Heil, C., Humphries, E., Lewitus, A., Magnien, R., Marshall, H., Sellner, K., Stockwell, D., Stoecker, D., Sudleson, M., 2008. Eutrophication and harmful algal blooms: a scientific consensus. *Harmful Algae* 8, 3–13. <https://doi.org/10.1016/j.hal.2008.08.006>.
- Hu, C., Lee, Z., Ma, R., Yu, K., Li, D., Shang, S., 2010. Moderate resolution imaging Spectroradiometer (MODIS) observations of cyanobacteria blooms in Taihu Lake, China. *J. Geophys. Res.* 115, C04002. <https://doi.org/10.1029/2009JC005511>.
- Hu, C., Barnes, B.B., Qi, L., Corcoran, A.A., 2015. A harmful algal bloom of *Karenia brevis* in the Northeastern Gulf of Mexico as revealed by MODIS and VIIRS: a comparison. *Sensors* 15, 2873–2887.
- Hunter, P.D., Tyler, A.N., Willby, N.J., Gilvear, D.J., 2008. The spatial dynamics of vertical migration by *Microcystis aeruginosa* in a eutrophic shallow lake: a case study using high spatial resolution time-series airborne remote sensing. *Limn. Oceanogr.* 53, 2391–2406.
- Johansen, R., Beck, R., Nowosad, J., Nietch, C., Xu, M., Shu, Y., Yang, B., Liu, H., Emery, E., Reif, M., Harwood, J., Young, J., Macke, D., Martin, M., Stillings, G., Stumpf, R., Su, H., 2018. Evaluating the portability of satellite derived chlorophyll-a algorithms for temperate inland lakes using airborne hyperspectral imagery and dense surface observations. *Harmful Algae* 76, 35–46.
- Jupp, D.L.B., Kirk, J.T.O., Harris, G.P., 1994. Detection, identification and mapping of cyanobacteria – using remote-sensing to measure the optical-quality of turbid inland waters. *Aust. J. Mar. Freshwat. Res.* 45 (5), 801–828.
- Kallio, K., 2000. Remote sensing as a tool for monitoring lake water quality. In: Heinonen, P., Ziglio, G., van der Beken, A. (Eds.), *Hydrological and Limnological Aspects of Lake Monitoring*. John Wiley & Sons, Ltd, Chichester, England, pp. 237–245.
- Kallio, K., Kutser, T., Hannonen, T., Koponen, S., Pulliainen, J., Vepsäläinen, J., et al., 2001. Retrieval of water quality from airborne imaging spectrometry of various lake types in different seasons. *Sci. Total Environ.* 268, 59–77. [https://doi.org/10.1016/S0048-9697\(00\)00685-9](https://doi.org/10.1016/S0048-9697(00)00685-9).
- Kneubuhler, M., Frank, T., Kellenberger, T.W., Pasche, N., Schmid, M., 2007. Mapping Chlorophyll-a in Lake Kivu with Remote Sensing Methods. Proceedings of the Envisat Symposium 2007, Montreux, Switzerland 23–27 April 2007 (ESA SP-636, July 2007).
- Koponen, S., Pulliainen, J., Kallio, K., Hallikainen, M., 2002. Lake water quality classification with airborne hyperspectral spectrometer and simulated MERIS data. *Remote Sens. Environ.* 79, 51–59.
- Kudela, R.M., Gobler, C.J., 2012. Harmful dinoflagellate blooms caused by *Cochlodinium* sp.: global expansion and ecological strategies facilitate bloom formation. *Harmful Algae* 14, 71–86.
- Kudela, R.M., Palacios, S.I., Austerberry, D.C., Accorsi, E.K., Guild, L.S., 2015a. Application of hyperspectral remote sensing to cyanobacterial blooms in inland waters, Torres-Perez, J. *Remote Sens. Environ.* 167, 1–10.
- Kudela, R.M., et al., 2015b. Harmful Algal Blooms. A Scientific Summary for Policy Makers. IOC/UNESCO, Paris (IOC/INF-1320).
- Lathrop, R.G., Lillesand, T.M., 1986. Use of thematic mapper data to assess water quality in Green Bay and Central Lake Michigan. *Photogr. Eng. Remote Sens.* 52, 671–680.
- Lathrop, R.G., Lillesand, T.M., Yandell, B.S., 1991. Testing the utility of simple multidate thematic mapper calibration algorithms for monitoring turbid inland waters. *Int. J. Remote Sens.* 12 (10), 2045–2063.
- Lee, Z., Ahn, Y.-H., Mobley, C., Arnone, R., 2010. Removal of surface-reflected light for the measurement of remote-sensing reflectance from an above-surface platform. *Opt. Express* 18, 26313–26324.
- Lillesand, T.M., Johnson, W.L., Deuell, R.L., Lindstrom, O.M., Miesner, D.E., 1983. Use of Landsat data to predict trophic status of Minnesota lakes. *Photogramm. Eng. Remote Sens.* 49, 219–229.
- Lindsey, R., Herring, D., 2001. Modis. pp. 1–23.
- Linkov, I., Satterstrom, F.K., Loney, D., Steevans, J.A., 2009. The Impact of Harmful Algal Blooms on USACE Operations. ANSRP Technical Notes Collection. ERDC/TN ANSRP-09-1. U.S. Army Engineer Research and Development Center, Vicksburg, MS.
- Lopez, C.B., Jewett, E.B., Dortch, Q., Walton, B.T., Hudnell, H.K., 2008. Scientific assessment of freshwater harmful algal blooms. Interagency Working Group on Harmful Algal Blooms, Hypoxia, and Human Health of the Joint Subcommittee on Ocean Science and Technology, DC, Washington.
- Matthews, M.W., Bernard, S., 2013. Characterizing the absorption properties for remote sensing of three small optically-diverse South African reservoirs. *Remote Sens.* 5, 4370–4404.
- Mishra, S., 2012. Remote Sensing of Cyanobacteria in Turbid Productive Waters, PhD Dissertation. Mississippi State University, USA.
- Mishra, S., Mishra, D.R., 2012. Normalized difference chlorophyll index: A novel model for remote estimation of chlorophyll-a concentration in turbid productive waters. *Remote Sens. Environ.* 117, 394–406.
- Mishra, S., Mishra, D.R., 2014. A novel remote sensing algorithm to quantify phycocyanin in cyanobacterial algal blooms. *Environ. Res. Lett.* 9 (11). <https://doi.org/10.1088/1748-9326/9/11/114003>.
- Mishra, S., Mishra, D.R., Schluchter, W.M., 2009. A novel algorithm for predicting PC concentrations in cyanobacteria: a proximal hyperspectral remote sensing approach. *Remote Sens.* 1, 758–775.

- Mishra, S., Mishra, D.R., Lee, Z.P., 2013. Bio-optical inversion in highly turbid and cyanobacteria dominated waters. *IEEE Trans. Geosci. Remote Sens.*, 51 <https://doi.org/10.1109/TGRS.2013.2240462>.
- Mittenzwey, K.-H., Ulrich, S., Gitelson, A.A., Kondratiev, K.Y., 1992. Determination of chlorophyll-a of inland waters on the basis of spectral reflectance. *Limn. Oceanography* 37, 147–149.
- Moore, G.K., 1980. Satellite remote sensing of water turbidity. *Hydrol. Sci.* 25 (4), 407–422.
- Nechad, B., Ruddick, K.G., Park, Y., 2010. Calibration and validation of a generic multisensor algorithm for mapping of total suspended matter in turbid waters. *Remote Sens. Environ.* 114, 854–866.
- Ogashawara, I., Misra, D.R., Mishra, S., Curtarelli, M.P., Stech, J.L., 2013. A performance review of reflectance based algorithms for predicting phycocyanin concentrations in inland waters. *Remote Sens.* 5, 4774–4798.
- Olmanson, L.G., Brezonik, P.L., Bauer, M.E., 2013. Airborne hyperspectral remote sensing to assess spatial distribution of water quality characteristics in large rivers: the Mississippi River and its tributaries in Minnesota. *Remote Sens. Environ.* 130, 254–265.
- O'Neil, J.M., Davis, T.W., Burford, M.A., Gobler, C.J., 2012. The rise of harmful cyanobacteria blooms: the potential roles of eutrophication and climate change. *Harmful Algae* 14, 313–334.
- Peltzer, E.T., 2015. Model 1 and model 2 regressions. <http://www.mbari.org/staff/etp3/regress.htm> (Last updated 18 May 2009, last accessed, 27 April 2015).
- Papoutsas, C., Akylas, E., Hadjimitsis, D., 2013. The spectral signature analysis of inland and coastal water bodies acquired from field spectro-radiometric measurements. *Proc. SPIE* 8795, 1–7.
- Pearl, H.W., Paul, V.J., 2012. Climate change: links to global expansion of harmful cyanobacteria. *Water Res.* 46 (5), 1349–1363. <https://doi.org/10.1016/j.watres.2011.08.002>.
- Picard, R., Cook, D., 1984. Cross-validation of regression models. *J. Am. Stat. Assoc.* 79 (387), 575–583.
- Pinero, G., Perelman, S., Guerschman, J.P., Paruleo, J.M., 2008. How to evaluate models: observed vs. predicted or predicted vs. observed. *Ecol. Model.* 216, 316–322.
- Potes, M., Costa, M.J., Salgado, R., 2012. Satellite remote sensing of water turbidity in Alqueva reservoir and implications on lake modelling. *Hydrol. Earth Syst. Sci.* 16, 1623–1633.
- Qi, L., Ma, R., Hu, W., L., S.A., 2014. Assimilation of MODIS chlorophyll-a data into a coupled hydrodynamic-biological model of Taihu Lake, *IEEE J. Sel. Top. Appl. Earth Obs. Remote Sens.*, 7, 1, 1623–1631.
- Qi, L., Hu, C., Cannizzaro, J., Corcoran, A.A., English, D., Le, C., 2015a. VIIRS observations of a *Karenia brevis* bloom in the Northeastern Gulf of Mexico in the absence of a fluorescence band. *IEEE Geosci. Remote Sens. Lett.* <https://doi.org/10.1109/LGRS.2015.2457773>.
- Qi, L., Hu, C., Duan, H., Zhang, Y., Ma, R., 2015b. Influence of particle composition on remote sensing reflectance and MERIS maximum chlorophyll index algorithm: examples from Taihu Lake and Chaohu Lake. *IEEE Geosci. Remote Sens. Lett.* 12 (5), 1136–1140. <https://doi.org/10.1109/LGRS.2014.2385800>.
- Raschka, S., 2016. R Scripts for General Data Analysis and Plotting. https://github.com/rasbt/R-snippets/blob/master/heatmaps/h2_default_clustering.R.
- Reif, M., 2011. Remote Sensing for Inland Water Quality Monitoring: A U.S. Army Corps of Engineers Perspective, Engineer Research and Development Center/Environmental Laboratory Technical Report (ERDC/EL TR)-11-13 (44 pages).
- Ruddick, K., Nechad, B., Neukermans, G., Park, Y., Doxaran, D., Sirjacobs, D., Beckers, J.-M., 2008. Remote Sensing of Suspended Particulate Matter in Turbid Waters: State of the Art and Future Perspectives, CDROM Proceedings of the Ocean Optics XIX Conference, Barga, 19, 1–12.
- Santini, F., Alberotanza, L., Cavalli, R.M., Pignatti, S., 2010. A two-step optimization procedure for assessing water constituent concentrations by hyperspectral remote sensing techniques: an application to the highly turbid Venice lagoon waters. *Remote Sens. Environ.* 114, 887–898.
- Schalles, J., Yacobi, Y., 2000. Remote detection and seasonal patterns of phycocyanin, carotenoid and chlorophyll-a pigments in eutrophic waters. *Arch. Hydrobiol.* 55 (Special Issues Advances in Limnology), 153–168.
- Shen, L., Xu, H., Guo, X., 2012. Satellite remote sensing of harmful algal blooms (HABs) and a potential synthesized framework. *Sensors* 12, 7778–7803.
- Shi, K., Zhang, Y., Zhou, Y., Liu, X., Zhu, G., Qin, B., Gao, G., 2017. Long-term MODIS observations of cyanobacterial dynamics in Lake Taihu: responses to nutrient enrichment and meteorological factors. *Sci. Rep.* 7, 40326. <https://doi.org/10.1038/srep40326>.
- Simis, S.G.H., Peters, S.W.M., Gons, H.J., 2005. Remote sensing of the cyanobacteria pigment phycocyanin in turbid inland water. *Limnol. Oceanogr.* 50, 237–245.
- Simis, S.G.H., Ruiz-Verdu, A., Dominguez, J.A., Pena-Martinez, R., Peters, S.W.M., Gons, H.J., 2007. Influence of phytoplankton pigment composition on remote sensing of cyanobacterial biomass. *Remote Sens. Environ.* 106, 414–427.
- Spear, S., 2014. Toxic algae bloom leaves 500,000 without drinking water in Ohio. EcoWatch, [\(https://www.ecowatch.com/toxic-algae-bloom-leaves-500-000-without-drinking-water-in-ohio-1881940537.html\)](https://www.ecowatch.com/toxic-algae-bloom-leaves-500-000-without-drinking-water-in-ohio-1881940537.html), (03 August 2014). Accessed 28 May, 2017.
- Stone, M., 1974. Cross-Validatory choice and assessment of statistical predictions. *J. R. Stat. Soc. Ser. B* 36 (1), 111–147.
- Stumpf, R.P., 2014. Satellite monitoring of toxic cyanobacteria for public health, Earthzine. <http://earthzine.org/2014/03/26/satellite-monitoring-of-toxic-cyanobacteria-for-public-health/>, Accessed date: 7 April 2016.
- Stumpf, R.P., Pennock, J.R., 1989. Calibration of a general optical equation for remote sensing of suspended sediments in a moderately turbid estuary. *J. Geophys. Res.* 94, 14363–14371.
- Stumpf, R.P., Wynne, T.T., Baker, D.B., Fahnstiel, G.L., 2012. Inter-annual variability of cyanobacterial blooms in Lake Erie. *PLoS One* 7, 1–11.
- Stumpf, R.P., Davis, T.W., Wynne, T.T., Graham, J.L., Loftin, K.A., Johengen, T.H., Gossiaux, D., Palladino, D., Burtner, A., 2016. Challenges for mapping cyanotoxin patterns from remote sensing of cyanobacteria. *Harmful Algae* 54, 160–173.
- Sun, D., Hu, C., Qiu, Z., Shi, K., 2015. Estimating phycocyanin pigment concentration in productive inland waters using Landsat measurements: a case study in Lake Dianchi. *Opt. Express* 23 (3), 1–19.
- Torbick, N., Hu, F., Zhang, J., Qi, J., Zhang, H., Becker, B., 2008. Mapping Chlorophyll-a concentrations in West Lake, China using Landsat 7 ETM+. *J. Great Lakes Res.* 34, 559–565.
- Trescott, A., 2012. Remote sensing models of algal blooms and cyanobacteria in Lake Champlain, Master's thesis. U. Massachusetts 1–48.
- U.S. Environmental Protection Agency (USEPA), 2001. Method 1684. Total, Fixed and Volatile Solids in Water, Solids, and Biosolids. EPA-821-R-01-015. Washington, DC.
- U.S. Environmental Protection Agency (USEPA), 2012. Cyanobacteria and cyanotoxins: Information for drinking water systems. EPA-810F11001. Environmental Protection Agency, Office of Water, U.S.
- U.S. Environmental Protection Agency (USEPA), 2016. Method 546: determination of total microcystins and nodularins in drinking water and ambient water by Adda enzyme-linked immunosorbent assay. EPA 815-B-16-011. Office of Ground Water and Drinking Water, Cincinnati, OH.
- U.S. Geological Survey, 2015a. Landsat-8 (L8) Data Users Handbook. pp. 1–98.
- U.S. Geological Survey, 2015b. Remote sensing applications. http://landsat.usgs.gov/remote_sensing_applications.php, Accessed date: 12 April 2016 (Last updated 07 February 2013).
- Verbyla, D.L., 1995. Satellite Remote Sensing of Natural Resources. CRC Lewis, p. 199.
- Vicory, A., March 26, 2009. Intergovernmental Cooperation and Public-Private Partnerships for Water Quality Management in the Ohio River Valley: The ORSANCO Experience. 26. Michigan State University stormwater workshop, p. 2009.
- Wells, M.L., Trainer, V.L., Smayda, T.J., Karlson, B.S.O., Trick, C.G., Kudela, R.M., Ishikawa, A., Bernard, S., Wulff, A., Anderson, D.M., Cochlan, W.P., 2015. Harmful algal blooms and climate change: learning from the past and present to forecast the future. *Harmful Algae* 49, 68–93. <https://doi.org/10.1016/j.hal.2015.07.009>.
- Wheeler, S.M., Morrissey, L.A., Levine, S.N., Livingston, G.P., Vincent, W.F., 2012. Mapping cyanobacterial blooms in Lake Champlain's Missisquoi Bay using QuickBird and MERIS satellite data. *J. Great Lakes Res.* 38, 68–75.
- Wozniak, M., Bradtke, K.M., Darecki, M., Krezel, A., 2016. Empirical model for phycocyanin concentration estimation as an Indicator of cyanobacterial bloom in the optically complex coastal waters of the Baltic Sea. *Remote Sens.* 8, 1–23.
- Wu, J.-L., Ho, C.-R., Huang, C.-C., Srivastav, A.L., Tzeng, J.-H., Lin, Y.-T., 2014. Hyperspectral sensing for turbid water quality monitoring in freshwater rivers: empirical relationship between reflectance and turbidity and total solids. *Sensors* 14, 22670–22688.
- Wynne, T.T., Stumpf, R.P., Tomlinson, M.C., Warner, R.A., Tester, P.A., Dyble, J., 2008. Relating spectral shape to cyanobacterial blooms in the Laurentian Great Lakes. *Int. J. Remote Sens.* 29, 3665–3672.
- Wynne, T.T., Stumpf, R.P., Tomlinson, M.C., Dyble, J., 2010. Characterizing a cyanobacterial bloom in western Lake Erie using satellite imagery and meteorological data. *Limnol. Oceanogr.* 55 (5), 2025–2036.
- Wynne, T.T., Stumpf, R.P., Tomlinson, M.C., Dyble, J., 2012. Characterizing a cyanobacterial bloom in western Lake Erie using satellite imagery and meteorological data. *Limnol. Oceanogr.* 55, 2025–2036.
- Wynne, T.T., Stumpf, R.P., Tomlinson, M.C., Fahnsteil, G.L., Schwab, D.J., Dyble, J., Joshi, S., 2013. Evolution of a cyanobacterial bloom forecast system in western Lake Erie: development and initial evaluation. *J. Great Lakes Res.* 39, 90–99.
- YSI, 2012. 6-Series Multiparameter Water Quality Sondes: User Manual. Environmental Monitoring Systems Operations Manual. YSI Incorporated, Yellow Springs, OH.
- Zhang, W.H., 1992. A preliminary study on seiches in Taihu Lake. *J. Lake Sci.* 4, 23–28 (In Chinese with English abstract).
- Zhang, C., Han, M., 2015. Mapping chlorophyll-a concentration in Laizhou Bay using Landsat 8 OLI data. Proceedings of the 36th IAHR World Congress. The Hague, The Netherlands 28 June–3 July.